5T8066

Convective Systems over the South China Sea: Cloud-Resolving Model Simulations

W.-K. Tao[1], C.-L. Shie[1,2], D. Johnson[1,2], J. Simpson[1], S. Braun[1], R. Johnson[3] and P. E. Ciesielski[3]

[1]*Laboratory for Atmospheres*
NASA/Goddard Space Flight Center
Greenbelt, MD 20771
USA

[2]*Goddard Earth Sciences and Technology Center*
University of Maryland, Baltimore County
Baltimore, MD

[3]*Department of Atmospheric Science*
Colorado State University
Fort Collins, CO 80523

J. Atmos. Sci.

(May 2002)

Corresponding author address: Dr. Wei-Kuo Tao, Mesoscale Atmospheric Processes Branch, Code 912, NASA/GSFC, Greenbelt, MD 20771
email: tao@agnes.gsfc.nasa.gov

Abstract

The South China Sea Monsoon Experiment (SCSMEX) was conducted in May-June 1998. One of its major objectives is to better understand the key physical processes for the onset and evolution of the summer monsoon over Southeast Asia and southern China. The two-dimensional version of the GCE model is used to simulate two SCSMEX convective periods [May 18-26 (prior to and during the monsoon) and June 2-11 (after the onset of the monsoon), 1998]. Observed large-scale advective tendencies for potential temperature, water vapor mixing ratio, and horizontal momentum are used as the main forcing in governing the GCE model in a semi-prognostic manner. The June SCSMEX case has stronger forcing in both temperature and water vapor, stronger low-level vertical shear of the horizontal wind and larger convective available potential energy (CAPE).

The temporal variation of the model-simulated rainfall compares quite well to that estimated from soundings. The time- and domain-averaged heating and moisture budgets are generally in good agreement with those diagnostically determined from soundings. However, the model results have a higher temporal variability. The model underestimates the rainfall by 17 to 20% compared to that based on soundings. The GCE-model-simulated rainfall for June is in very good agreement with the TRMM PR and GPCP, but not the TMI. A single-peaked rainfall probability distribution is well simulated by the model for the June case, but the model does not capture an observed bimodal rainfall distribution in May.

Cloud-cloud interactions and mergers are common features in the model simulations. Two types of organized convective systems, unicell (May case) and multi-cell (June case), are simulated by the model. They are determined by the observed mean U-wind shear (uni-directional versus reverse shear profiles above midlevel). Convection is more vigorous and has a higher temporal variation in June than May. The convective heating is also stronger and occurs at a higher altitude in convective systems in June. The cooling in the stratiform region is also much stronger in June than in May. Overall, the model agrees better with observations for the June case rather than the May case.

By examining the surface energy budgets, the model results show that the two largest terms for both cases are net condensation (heating/drying) and imposed large-scale forcing (cooling/moistening). These two terms are opposite in sign, however. The model results also show that there are more latent heat fluxes prior to the onset of the monsoon (May case). However, more rainfall is simulated after the onset of the monsoon (June case). Net radiation (solar heating and longwave cooling) can contribute about 34% and 25%, respectively, of the net condensation

(condensation minus evaporation) for the May and June cases. Sensible heat fluxes do not contribute to rainfall in either of the SCSMEX cases.

Several sensitivity tests are performed to examine the impact of the radiation, microphysics and large-scale mean horizontal wind on the organization and intensity of the SCSMEX convective systems. Total rain production is reduced by about 17-18% in the ice-free runs. The model results are also sensitive to ice processes and cloud-radiation interaction. The large-scale mean horizontal wind plays an important role in the organization of cloud system but not the precipitation processes.

The SCSMEX model results are compared to other GCE-model-simulated convective systems that developed during other field campaigns (i.e., TOGA COARE, GATE and ARM). Large-scale advective forcing in temperature and water vapor is the major energy source for net condensation in the tropical cases. Large-scale cooling exceeds large-scale moistening in the TOGA COARE and GATE cases. For SCSMEX, however, there is more large-scale moistening than cooling. However, net radiation and sensible and latent heat fluxes play a much more important role in the three ARM cases.

1. Introduction

The global hydrological cycle is central to climate system interactions and the key to understanding their behavior. Rainfall and its associated precipitation processes are a key link in the hydrologic cycle. Fresh water provided by tropical rainfall and its variability can exert a large impact upon the structure of the upper ocean layer. In addition, two-thirds of the global rain falls in the tropics, while the associated latent heat release accounts for three-fourths of the total heat energy for the Earth's atmosphere. The Tropical Rainfall Measuring Mission (TRMM), a joint U.S./Japan space project, is a satellite mission that can provide an adequate measurement of rainfall as well as estimate the four-dimensional structure of diabatic heating over the global tropics using an inclined low-altitude orbit and a combination of precipitation radar, VIS/IR and microwave radiometers (Simpson *et al.* 1988). The distributions of rainfall and inferred heating can be used to advance our understanding of the global energy and water cycle. In addition, this information can be used for global circulation and climate models for testing and improving their parameterizations.

Cloud-resolving (or cumulus ensemble) models (CRMs) are one of the most important tools used to establish quantitative relationships between diabatic heating and rainfall. This is because latent heating is dominated by phase changes between water vapor and small, cloud-sized particles, which can not be directly detected using remote sensing techniques. The CRMs, however, explicitly simulate the conversion of cloud condensate into raindrops and various forms of precipitation ice. It is these different forms of precipitation that are most readily detected from space, and which ultimately reach the surface in the form of rain. The Goddard Cumulus Ensemble (GCE) model is a cloud-resolving model. It has been used to provide cloud data sets associated with various types of clouds/cloud systems from different geographic locations for the TRMM retrieval algorithm database (see a review by Simpson *et al.* 1997). The data represent instantaneous values and are selected from periods, where the cloud and precipitation fields meet predetermined characteristics that are unique or complementary to the database requirements. The output quantities provided include: pressure, temperature, relative humidity, rain rate, hydrometeor (cloud water, ice, rain, snow, and graupel) mixing ratios, vertical velocity, latent heating, hydrometeor drying, vertical eddy heat and moisture flux convergence, radiative heating, and convective/stratiform classification.

Several field campaigns (FCs) conducted during 1998 and 1999 were aimed at the validation of TRMM products (i.e., rainfall and the vertical distribution of latent heating). Since latent heating profiles cannot be directly measured, cloud-resolving models (CRMs) are used in TRMM algorithms to provide a link between the latent heating profiles, TRMM radar and

radiometer observations. Consequently, one of the key components of the TRMM FCs is to provide observations of the structure and evolution of MCSs, individual convective clouds and their embedded large-scale environment. CRMs require these data sets for initial conditions as well as for the validation of their vertical latent heating structure. The South China Sea Monsoon Experiment (SCSMEX) was one of four major TRMM FCs and was conducted in May-June 1998. One of its major objectives is to better understand the key physical processes for the onset and evolution of the summer monsoon over Southeast Asia and southern China (Lau *et al.* 2000). Multiple observation platforms (e.g., soundings, Doppler radar, ships, wind profilers, radiometers, etc.) during SCSMEX provided a first attempt at investigating the detailed characteristics of convection and circulation changes associated with monsoons over the South China Sea region. SCSMEX also provided precipitation derived from atmospheric budgets (Johnson and Ciesielski 2002) and dual Doppler radar (Rickenback *et al.* 1998) for comparison to those obtained from the Tropical Rainfall Measuring Mission (TRMM).

The use of cloud-resolving models (CRMs) in the study of tropical convection and its relation to the large-scale environment can be generally categorized into two methodologies. The first approach is so-called "*cloud ensemble modeling*". In this approach, many clouds/cloud systems of different sizes in various stages of their lifecycles can be present at any model simulation time. The large-scale effects that are derived from observations are imposed into the models as the main forcing, however. In addition, the cloud ensemble models use cyclic lateral boundary conditions (to avoid reflection of gravity waves) and require a large horizontal domain (to allow for the existence of an ensemble of clouds). The clouds simulated from this approach could also be termed "*continuous large-scale forced convection*". The advantage of this approach is that the modeled convection will be forced to almost the same (but not identical) intensity, thermodynamic budget and organization as the observations. This approach will also allow the cloud-resolving model to perform multi-day or multi-week time integration. On the other hand, the second approach for cloud-resolving models usually requires initial temperature and water vapor profiles that have a medium to large convective available potential energy (CAPE), and an open lateral boundary condition is used. The modeled clouds, then, are initialized with either a cool pool, warm bubble or surface processes (i.e., land/ocean fluxes). These modeled clouds could be termed "*self-forced convection*". The key developments in the cloud ensemble modeling using the continuous large-scale forced convection approach over the past two decades were listed in Table 1 in Johnson *et al.* (2002) and Tao (2003).

In this paper, the GCE model will be used to perform two multi-day integrations using SCSMEX data using the first approach. The first one is prior to and during the monsoon onset period

(May 18-26, 1998), and the second is after the onset of the monsoon (June 2 – 11, 1998). The objectives of this modeling paper are: (1) to examine the characteristics of surface rainfall in the convective and stratiform regions, (2) to calculate and examine the vertical distribution of the latent heating and its structure in the convective and stratiform regions, (3) to examine the microphysical processes (i.e., condensation/evaporation, deposition/sublimation, and melting/freezing), and (4) to compute and analyze the thermodynamic budgets (domain averaged) and surface budget. The similarities and differences prior to, during and after the onset of the monsoon will be discussed. The results are also compared to those from other FCs (i.e., GATE, TOGA COARE and DOE/ARM[1]). In addition, the impact of microphysical processes, radiation and the vertical shear of the horizontal wind on model results will be examined through sensitivity tests.

2. Large-Scale Environmental Conditions

Johnson and Ciesielski (2002) calculated the apparent heat source (Q_1) and apparent moisture sink (Q_2) which can be used to validate TRMM rainfall products. In addition, the horizontal and vertical advective components in Q_1 and Q_2 can be used as large-scale advective forcing for the CRMs (Soong and Tao 1980; Moncrieff *et al.* 1997). Two major convective events around 18-26 May and 2-11 June 1998 were identified and selected for model simulation. The first event is prior to and during the onset of the monsoon; the second is post onset. Figure 1 shows the time series of large-scale advective forcing in temperature and water vapor associated with these two SCSMEX events that were used for the GCE model simulations. Both cases show a similar order of magnitude of peak heating, 22-26 K day^{-1} between 350 and 500 mb. However, the mean large-scale forcing associated with these two cases is quite different (Fig. 2). The June case has stronger forcing in both temperature and water vapor. In addition, the temperature forcing is located higher in the June case compared to the May case. The large-scale forcing in water vapor is much stronger in the lower and middle troposhere in the June case. Also, the large-scale forcing in water vapor has more complex vertical structures (multi-peaks) in SCSMEX compared to those of GATE and TOGA COARE (single peaks located at low to middle altitude).

The observed time series of mean zonal, meridional and vertical wind are shown in Figs. 3 and 4, respectively. Differences between these two periods are quite significant. There is stronger low-level vertical shear in the u-wind component during the June period. This may indicate that convection is more organized in June. The mean vertical velocity is stronger and at a higher altitude

---

[1] GATE stands for Global Atmospheric Research Programme (GARP) Atlantic Experiment. TOGA-COARE stands for Tropical Ocean-Global Atmosphere Program - Coupled Ocean-Atmosphere Response Experiment. DOE/ARM stands for Department of Energy Atmospheric Radiation Measurement Program.

in June. This feature is consistent with the large-scale advective forcing in temperature and water vapor because the vertical advection term in the Q_1 and Q_2 budgets is always much larger than its horizontal counter part for deep convective events in the tropics (i.e., Soong and Tao 1980). The u-wind component is quite different between an active convective period (i.e., May 18-22) and in-active one (May 22-24). The wind changed from westerly to easterly at lower and upper troposphere around May 22. There are about six and eight-nine major convective events, respectively, shown in the large-scale advective forcing in temperature and water vapor, and large-scale mean vertical velocity for the May and June cases.

Table 1 compares several characteristics of the large-scale flow (stability, lifted index, precipitable water and Richardson number) in which these two SCSMEX systems were embedded. The vertically integrated water vapor contents are quite moist (62.58 and 62.34 g cm^{-2}, respectively) for both two cases. A very moist environment in the Pacific region (WMONEX, AMEX and TOGA COARE) is quite a common feature. The Richareson number is larger in the June case because of the stronger U-wind shear. The CAPE and lifted index are also larger in the June period (1324 m^2 s^{-2} and -1.92) than in the May one (825 m^2 s^{-2} and -0.91).

3. The Goddard Cumulus Ensemble (GCE) Model and Model Set-ups

3.1 The GCE model

The model used in this study is the two-dimensional (2-D) version of the Goddard Cumulus Ensemble (GCE) model. The equations that govern cloud-scale motion (wind) are anelastic by filtering out sound waves The subgrid-scale turbulence used in the GCE model is based on work by Klemp and Wilhelmson (1978). In their approach, one prognostic equation is solved for subgrid kinetic energy, which is then used to specify the eddy coefficients. The effect of condensation on the generation of subgrid-scale kinetic energy is also incorporated in the model (see Soong and Ogura 1980; Tao and Soong 1986 for details). The cloud microphysics include a parameterized Kessler-type two-category liquid water scheme (cloud water and rain), and a parameterized Lin *et al.* (1983) or Rutledge and Hobbs (1984) three-category ice-phase scheme (cloud ice, snow and hail/graupel) (see Tao and Simpson 1993 and Tao *et al.* 2002 for a detailed description of the cloud microphysics). Shortwave (solar) and longwave (infrared) radiation parameterizations are also included in the model (Tao *et al.* 1996). The TOGA-COARE[2] bulk flux algorithm (Fairall *et al.*

---

2 TOGA COARE was conducted in the equatorial Pacific region during 1992-1993. Its major objective was to gain a better understanding of the principal role of the western Pacific Ocean warm pool in oceanic and atmospheric (coupling) processes (Webster and Lucas, 1992).

1995) is linked to the GCE model for calculating the surface fluxes (Wang *et al.* 1996, 2002). All scalar variables (potential temperature, mixing ratio of water vapor, turbulence coefficients, and all five hydrometeor classes) use forward time differencing and a positive definite advection scheme with a non-oscillatory option (Smolarkiewicz and Grabowski, 1990). The dynamic variables, u, v and w, use a second-order accurate advection scheme and a leapfrog time integration (kinetic energy semi-conserving method). Details of the GCE model description and improvements can be found in Tao *et al.* (2002).

For the present study, a stretched vertical coordinate with 41 levels is used. The model has finer resolution (about 80 meters) in the boundary layer and coarser resolution (about 1000 meters) in the upper levels. The grid spacing in the horizontal plane is 1000 meters with 512 grid points. The time step is 7.5 s. Surface fluxes from the ocean and cloud-radiation interactive processes are explicitly included in this study. The observed sea surface temperature was used for latent and sensible heat flux calculations.

3.2 *Model set-up for imposing the large-scale advective forcing*

Observed large-scale advective tendencies (or forcing) of potential temperature, water vapor mixing ratio, and horizontal momentum (Figs. 1 and 3) are used as the main large-scale forcing in governing the GCE model in a semi-prognostic manner (Soong and Ogura 1980; Soong and Tao 1980; Tao and Soong 1986; and many others). The major characteristic of this approach is that ensembles of clouds can be generated by the "*observed-prescribed forcing*". The large-scale advective tendencies for potential temperature and water vapor mixing ratio q,

$$\left[\frac{\partial\overline{\theta}}{\partial t}\right]_{L.S.} = -\overline{v}\cdot\nabla\overline{\theta} - \overline{w}\frac{\partial\overline{\theta}}{\partial z}$$

and

$$\left[\frac{\partial\overline{q}}{\partial t}\right]_{L.S.} = -\overline{v}\cdot\nabla\overline{q} - \overline{w}\frac{\partial\overline{q}}{\partial z}$$

were derived every six hours over the SCSMEX analyses. Since accurate calculations of the large-scale horizontal momentum forcing terms are difficult to obtain from observations in the tropics, these terms were instead replaced by a nudging term:

$$\left[\frac{\partial\overline{v}}{\partial t}\right]_{L.S.} = -\frac{\overline{v}-\overline{v}_{obs}}{\tau}$$

where $\overline{v}$ is the model domain averaged horizontal velocity, $\overline{v}_{obs}$ is the observed large-scale

horizontal velocity, and τ is the specified adjustment time scale (one hour). This method constrains the domain-averaged horizontal velocities to follow the observed values, and thereby provides a simple means to controlling the cloud system dynamics by the large-scale momentum and shear. Cyclic lateral boundary conditions were incorporated to ensure that there was no additional heat, moisture or momentum forcing inside the domain apart from the large-scale forcing (Soong and Tao 1980; Tao and Soong 1986). This type of cloud-resolving modeling was used by many recent modeling studies for studying GATE and TOGA COARE convective systems (Krueger 1988, Grabowski *et al.* 1998, Wu and Randall 1996, Wu *et al.* 1998, Donner *et al.* 1999). Please see breif reviews by Johnson *et al.* (2002).

3.3 *Convective-stratiform partitioning method*

In the GCE model convective-stratiform partitioning method, convective, stratiform and non-surface precipitation regions are identified using the information from surface rainrates first (Churchill and Houze 1984). Two additional criteria are applied which have been included to identify regions where convection may be quite active *aloft* though there is little or no precipitation yet at the surface, such as areas associated with tilted updrafts and *new cells* initiated ahead of an organized squall line (Tao and Simpson 1989; Tao *et al.* 1993a). Non-surface precipitation regions are considered to be convective if cloud water exceeds a certain threshold (i.e., the minimum of either 0.5 g kg^{-1} or half of the maximum cloud water at that specific simulation time), or if the updraft exceeds a certain threshold (i.e., the minimum value between 3 m s^{-1} and half of the maximum updraft at that specific simulation time) below the melting level. The presence of this amount of cloud water is a good indication of a saturated area (100% relative humidity). Chin (1994), Cotton (1998, personal communication) and Redelsperger *et al.* (1999) have adopted this method. Different convective and stratiform separation techniques (i.e., Churchill and Houze 1984, Tao *et al.* 1993a, Xu 1995, Caniaux 1994, and Steiner *et al.* 1995) were examined and compared by Lang *et al.* (2002). Overall, it was found that the different separation techniques produced results that qualitatively agreed. However, the quantitative differences were significant. Overall, Churchill and Houze (1984), Tao *et al.* (1993), and Xu (1995) were found to produce the most stratiform results and Steiner *et al.* (1995) the most convective.

4. Results

4.1 *Surface Rainfall Characteristics*

Figures 5 (a) and (b) show the time series of the GCE model simulated surface rain rate for two

SCSMEX convective periods, May 18-26 (prior to and during the monsoon) and June 2-11 (after the onset of the monsoon), 1998. Ensembles of clouds and cloud systems with various sizes are simulated by the model as expected. The majority of the simulated convective systems propagated from east to west in both cases. However, the convective systems in the May case propagated slower than those in the June case. In addition, cloud-cloud interactions and merging are a more common feature for the May period. These cloud-cloud interactions can influence the direction of propagation of individual clouds and cloud systems. Some of the convection simulated in the May case exhibits characteristics that are quite similar to those of unicell convection as discussed in Dudhia *et al.* (1987). The mean U-wind shear in the May SCSMEX case [Fig. 4(a)] does not reverse sign above mid-levels (3-5 km level) as while the June case. With a uni-directional shear profile of the U-wind, the model simulates unicell type convection (Dudhia *et al.* 1987; Tao *et al.* 1995). On the other hand, the model can produce multi-cell type convection with the reversing shear profile in the June case.

Figure 6 shows the hydrometeor content (ice and water), equivalent potential temperature deviation, storm relative-horizontal wind, and the w-velocity associated with two types of organized, long-lived convective systems simulated during the May and June periods. In general, these types of convective systems can contribute significant amounts of surface rainfall and associated latent heating. The simulated cloud system shown in Figs. 6(a) to 6(d) reproduces qualitatively several important features typically associated with tropical squall systems (Houze 1997; Zipser 1979). For example, narrow convective cores are located at the leading edge of the system with a widespread trailing stratiform region. The upshear tilt of the core updrafts and a rear inflow extending from the middle troposphere to the leading edge of the cool pool are well simulated. In addition, a strong cold pool associated with a squall meso-high and a wake low are also present in the simulation. Note that there is also a new, shallower convective updraft developing within the cool pool region. It is caused by the surface fluxes from ocean. Figs. 6(e) to 6(h) show the unicell type of convection that was simulated in the May case. It has characteristics of a single updraft, much less stratiform cloud coverage, and a mesoscale circulation that is weaker than in the squall type of convection. The cool pool is much weaker and less organized than in the organized type of convection.

Figure 7 shows time series of rainfall rates averaged over the SCSMEX region that were simulated by the GCE model and estimated from soundings. The temporal variation of the GCE model simulated rainfall is in very good agreement with that estimated from soundings (Johnson and Ciesielski 2002). No rainfall was simulated before and during May 23 as observed. The good agreement is mainly caused by the fact that the GCE model was forced by large-scale tendencies in

temperature and water vapor computed from the sounding network. When the imposed large-scale advective forcing cools and moistens the environment, the model responds producing clouds through condensation and deposition. The fall out of large precipitation particles produces rainfall at the surface. The larger the advective forcing, the larger the microphysical response (rainfall) the model will produce (Soong and Tao 1980; Tao and Simpson 1984). On the other hand, the model will not produce any cloud nor rainfall when the imposed large-scale advective forcing heats and dries the atmosphere.

Rainfall probability distributions, both simulated and estimated by soundings, for these two SCSMEX cases are shown in Fig. 8. In the May case, a bimodal distributions, with the first peak centered at 0.9 mm h^{-1} and second at 1.76 mm h^{-1}, is estimated by the sounding, but not simulated by the model. In contrast, there is only a single peak centered at 1.13 mm h^{-1} for both simulated and observed distributions for the June case. The GCE model results also indicate that there is more light rain (less than 1 mm h^{-1}), both simulated and observed in May case. The weaker large-scale advective forcing in May produced more light rainfall. Wind shear (of u-wind) can also play an important role in determining the rainfall distribution.

The rainfall amounts from the GCE model, soundings, the TRMM Precipitation radar (PR), TMI and GPCP are shown in Table 2. All they indicate that less rainfall occurs in the May case than in the June case. Surprisingly, the model under-estimated rainfall by 17% and 20%, respectively, for the May and June cases compared to that calculated based on soundings. It is unclear why the model under-estimated rainfall even though the GCE model was forced by large-scale tendencies in temperature and water vapor computed from the sounding network. Two additional sources of forcing, ocean surface fluxes and radiation, could be under-estimated by the model. The model physics may be another reason for this discrepancy. Accurate and consistent large-scale advective tendencies in temperature and water vapor are also needed for CRM simulation. Tao *et al.* (2000) found that the large-scale advective terms for temperature and water vapor are not always consistent. For example, large-scale forcing could indicate strong drying (which would produce cooling in the model through evaporation) but not contain large-scale advective heating to compensate. This discrepancy in forcing would cause differences between the observed and modeled rainfall. Table 2 also shows that the GCE-model-simulated rainfall for June is in very good agreement with the TRMM PR and GPCP. The TMI-estimated rainfall is about twice that estimated by the GCE and PR. A detailed study to determine the reasons for the differences in rainfall amounts between the different measurements is underway through the TRMM project.

The smaller large-scale advective forcing in temperature and water vapor, and the U-wind shear profile for the May case produce more light precipitation that is categorized as stratiform than those in the June case (see Fig. 8). That is why more stratiform rain is simulated in the May case than the June case (Table 2). It is known that stratiform rain amounts are typically about 40-50% in organized convective systems in the tropics (Houze 1997). This implies that GCE estimated stratiform amounts could all be reasonable for both cases. There is a relatively small difference (less than 7%) in stratiform percentage between the model and TRMM (both PR and TMI) for the June case compared to the May case (over 13%). Sampling could also be the reason for the difference between the model and TRMM estimates.

4.2 *Vertical distribution of Q1 and Q2 budget*

In diagnostic studies (*e.g.*, Yanai *et al.* 1973), it is customary to define the apparent heat source Q_1 and the apparent moisture sink Q_2 of a large-scale system by averaging horizontally the thermodynamic and water vapor equations as:

$$Q_1 = \overline{\pi}[\frac{\partial \overline{\theta}}{\partial t} + \overline{\vec{V}} \bullet \nabla \overline{\theta} + \overline{w}\frac{\partial \overline{\theta}}{\partial z}] + \overline{Q}_R, \tag{1}$$

$$Q_2 = -\frac{L_v}{C_p}[\frac{\partial \overline{q}_V}{\partial t} + \overline{\vec{V}} \bullet \nabla \overline{q}_V + \overline{w}\frac{\partial \overline{q}_V}{\partial z}]. \tag{2}$$

Q_1 and Q_2 can be calculated either from observations or from grid values in a large- or regional-scale prediction model. Q_1 and Q_2 can directly relate to the contributions of cloud effects which can be explicitly estimated by CRMs (Soong and Tao 1980; Tao and Soong 1986; Krueger 1988; Tao *et al.* 1993a and many others):

$$Q_1 = \overline{\pi}[-\frac{1}{\overline{\rho}}\frac{\partial \overline{\rho} w'\theta'}{\partial z} - \vec{V}' \bullet \nabla \theta' + D_\theta] + \frac{L_v}{C_P}(c-e) + \frac{L_f}{C_P}(f-m) + \frac{L_s}{C_P}(d-s) + Q_R \tag{3}$$

$$Q_2 = \frac{L_v}{C_P}[\frac{1}{\overline{\rho}}\frac{\partial \overline{\rho} w' q_V'}{\partial z} + \vec{V}' \bullet \nabla q_V' + D_{q_V}] + \frac{L_v}{C_P}(c-e) + \frac{L_s}{C_P}(d-s) \tag{4}$$

The overbars denote horizontal averages, and the primes indicate deviations from the horizontal averages. The variable $\overline{\rho}$ is the density, and $\overline{\pi} = (p/P_o)^{R/C_P}$ is the nondimensional pressure, where P is the dimensional pressure and P_{oo} the reference pressure taken to be 1000 mb. C_p is the specific heat of dry air at constant pressure, and R is the gas constant for dry air. The variables L_v, L_f and L_s are the latent heats of condensation, fusion and sublimation, respectively. The variables c, e, f, m, d and s stand for the rates of condensation, evaporation of cloud droplets and raindrops, freezing of raindrops, melting of snow and graupel/hail, deposition of ice particles and sublimation of ice particles, respectively. The term Q_R is the cooling/heating rate associated with radiative

processes. Also, the first terms on the right-hand side of (3) and (4) are the vertical eddy heat and moisture flux convergence, respectively.

Time series of the apparent heat source Q_1 diagnostically determined by soundings and explicitly calculated in the GCE model for the period May 18 - May 26, 1998 are illustrated in Figs. 9(a) and (b). The pattern of temporal variability corresponds well between the heating and the surface rainfall both for the soundings estimated and the GCE model. The model results, however, show more temporal variability. This is perhaps caused by the fact that diagnostically determined Q_1 was calculated using 6-hourly soundings. The GCE model estimates are based on 2-minute statistics of cloud processes (i.e., condensation, evaporation, deposition and sublimation, melting and freezing rates). The GCE model did not capture the deep convection that occurred after May 24. This is because strong heating and drying are imposed at lower and middle levels (see Fig. 1) from the large-scale advective forcing during the period May 23 and 24 inhibiting the subsequent development of deep convection. However, this is not the main reason for the disagreement in rainfall between the model and the sounding estimates. The model consistently underestimates the daily rainfall. Figures 9(c) and (d) show the time series of the GCE modeled Q_1 in the convective and stratiform regions, respectively, during the period May 18 - May 26, 1998. The typical convective and stratiform heating structures (or shapes) discussed in Houze (1997) and Johnson (1984) are captured by the GCE model. For example, the convective profiles show heating throughout the troposphere with a simple maximum around 500-550 mb. In the stratiform region, heating is maximized in the upper troposphere (around 400 mb) while cooling prevails below the melting level.

Time series of the apparent heat source, Q_1, diagnostically determined and calculated from the GCE model for the period June 2 - 11, 1998 are shown in Fig. 10. There is also good agreement in terms of temporal variation related to major convective events is found between the GCE simulation and the diagnostic sounding budget for the June period. The maximum heating peak in the upper troposphere (above the 400 mb level) mainly occurred in the stratiform region [Fig. 10(d)]. The results from the GCE model also show more temporal structure than that diagnostically determined as May case. Model results indicate that there is no cooling below the freezing level for the convective event on June 6-7. This is due to the strong moistening imposed by the large-scale advective forcing on June 6 [Fig. 1 (c)] while suppress the cooling from evaporation processes. Model results also indicate that there is stronger heating aloft and stronger cooling below in the stratiform region for both May and June cases [see Figs. 9(d) and 10(d)]. The cooling in the lower troposphere is from the evaporation of rain. The heating aloft is from deposition processes. Generally, stronger deposition can generate more ice particles and more melting from ice to rain. More evaporative

cooling can occur with more rain.

Figures 11 and 12 respectively, show the time series of the apparent moisture sink, Q_2, diagnostically determined by soundings and explicitly calculated from the GCE model for the period May 18 - May 26, 1998 and the period June 2-11, 1998. As with the Q_1 budget, the model simulations capture the temporal variation of the observed Q_2 in both cases. Again, the GCE model failed to produce the strong drying that occurred on May 23-24 as Q_1 budget. The typical convective and stratiform Q_2 structures (or shapes) discussed in Houze (1997) and Johnosn (1984) are also captured by the GCE model. Drying in the convective region due to the condensation/deposition processes (deplete moisture). The drying aloft and moistening (caused by evaporation) below occur in the stratiform region. Note that a drying was simulated in the planetary boundary layer in the stratiform region [Figs. 11(d) and 12(d)]. In the boundary layer, the large-scale advective forcing in water vapor and latent heat fluxes from ocean is to provide moisture (Fig. 1). Many shallow clouds are formed due to this moistening effect in both cases.

Time averaged heating and moisture budgets for the two SCSMEX cases are shown in Fig. 13. The budgets diagnostically determined from soundings are also shown for comparison. For May case, model simulated Q_1 has a higher maximum heating level than observation. Because a higher stratiform percentage can produce a higher maximum heating level (Johnson 1984; Tao *et al.* 1993b). This implies that the model could overestimate stratiform percentage in May case. Note that both PR and TMI estimate less stratiform rain compared to model simulated. The June case has a better agreement with observation than May case. Also note that the GCE simulated latent heating profile is in good agreement with the sounding estimated for June case but not for May case even though the rainfall amounts differ from observations in both cases. Overall, model simulation has a better agreement with observed in Q_2 than the Q_1 budget. The typical convective and stratiform heating/drying structures (or shapes) discussed in Houze (1997) and Johnson (1984) are well captured in the model except a large drying in the stratiform region at lower levels. Abundant shallow convection in the planetary boundary layer causes a large drying in the stratiform region for both cases [Figs. 13(c) and (d)].

Figures 14(a) and (b) show the net condensation, the net radiation, vertical eddy heat flux convergence in the Q_1 budget for both May and June cases. The vertical eddy flux convergence term includes both cloud-scale and sub-grid-scale (turbulence) effects. The local change term in temperature and the large-scale advective forcing in temperature are also shown. The net condensation and the large-scale forcing are the largest terms and are in opposite. The net condensation heating is simply a response to the imposed cooling by the large-scale advective

forcing. The net radiation is cooling that is about 20 to 30% of condensation heating. The eddy heat flux convergence is basically to re-distribute heat vertically and it can not be neglected in Q_1 budget in middle level (5 km level). This feature is related to the localized cooling by the melting processes. The eddy heat flux is to transport heat into the melting layer to compensate the loss of heating from melting process. This eddy transport term can also transport heat above melting caused by the localized freezing processes [i.e., Fig. 14(b)]. More melting and freezing in the June case produce a larger eddy heat fluxes convergence. Previous model results indicated that the eddy heat flux convergence term in temperature is very small except below cloud base compared to other terms (Soong and Tao 1980; Tao and Soong 1986; Krueger 1988). The lack of ice processes in previous modeling studies is the reason for this difference. The local change in temperature is quite small (at least an order smaller than both net condensation and large-scale advective forcing).

For the Q_2 budget, the GCE model results indicated that the net condensation and the imposed large-scale advective water vapor are in opposite. The vertical eddy convergence/divergence of moisture by clouds is quite important for Q_2 budget. It simply transports moisture from lower to upper troposphere. The vertical eddy convergence term is the same magnitude as the large-scale advective forcing above 8-km level. The vertical eddy convergence term is larger for the June case. Also, it produces very large drying in the lower troposphere that counteracts the large-scale moistening effect. The eddy moisture flux convergence also has a local maxima at middle levels [i.e., Fig. 14(d)]. This feature is in response to a maximum in condensation (loss of moisture) (see Fig. 15). The larger contribution of the vertical eddy convergence/divergence term in the Q_2 (water vapor) than the Q_1 (temperature) budgets is the major reason for Q_1 and Q_2 de-coupling (the level of maximum values in the Q_1 and Q_2 profiles is not at the same level). This result is consistent with many previous clouds modeling studies.

Figure 15 shows the simulated individual domain- and time-average accumulated microphysical processes (condensation, evaporation, deposition, sublimation, melting and freezing) associated with May and June cases. Both condensation and evaporation are the largest terms in both cases. The deposition and sublimation are dominant processes at upper troposphere. The evaporation and sublimation, respectively, is about one third of condensation and deposition. Both melting and freezing are small compared to condensation, evaporation, deposition and sublimation. However, the melting is the process responsible to a local minimum of net condensation heating [Figs. 14(a) and (b)] even though the condensation show a maximum at 5-km level.

There are several differences between the May and June cases. The first one is that convection is more vigorous and has a higher temporal variation in June than May. The convective

heating is stronger and occurs at a higher altitude in convective systems in June. The cooling in the stratiform region is also much stronger in June than in May. This is because the convective systems have more mesoscale organization in June (Fig. 6). All terms in Q_1 and Q_2 budget are larger in the June case than May case as expected. The large-scale advective forcing and the vertical shear of u-wind in the low troposphere are stronger in June than May. This is another major reason for the difference between the two cases.

4.3 Surface energy budgets

Horizontal and vertical integration of the equations for temperature, water vapor (q_v), and moist static energy h ($h = CpT + L_v q_v + gz$) over the entire model domain yields

$$C_p < \frac{\partial \overline{T}}{\partial t} > = < L_v(\bar{c} - \bar{e}) + L_f(\bar{f} - \overline{m}) + L_s(\bar{d} - \bar{s}) > - C_p < \frac{\partial \overline{\theta}}{\partial t} >_{L.S} + \overline{Q}_R + C_p \overline{H}_s \qquad (5)$$

$$L_v < \frac{\partial \overline{q}_v}{\partial t} > = - < L_v(\bar{c} - \bar{e}) + L_s(\bar{d} - \bar{s}) > + L_v < \frac{\partial \overline{q}_v}{\partial t} >_{L.S} + L_v \overline{E}_o \qquad (6)$$

$$< \frac{\partial \overline{h}}{\partial t} > = < L_f(\bar{f} - \overline{m}) + (L_s - L_v)(\bar{d} - \bar{s}) > - (C_p < \frac{\partial \overline{\theta}}{\partial t} >_{L.S} + L_v < \frac{\partial \overline{q}_v}{\partial t} >_{L.S}) + \overline{Q}_R + C_p \overline{H}_s + L_v \overline{E}_o \qquad (7)$$

where $-< \frac{\partial \overline{\theta}}{\partial t} >_{L.S}$ and $-< \frac{\partial \overline{q}_v}{\partial t} >_{L.S}$ are the large-scale advective cooling and moistening; E_O and H_S are the latent and sensible heat fluxes from the ocean surface. The physical processes responsible for the precipitation processes in each case can be quantified by examining the budget. In addition, the similarities and differences in terms of large-scale forcing, surface fluxes and radiation upon precipitation (net condensation) between two cases can be identified.

Table 3 lists the temperature budget for both May and June cases. In both runs, the largest two terms in the temperature budget are net condensation (heating) and imposed large-scale forcing (cooling). These two terms are opposite in sign, however. This is also true for the water vapor budget (Table 4). Soong and Tao (1980) performed experiments with different magnitudes of large-scale forcing and found that the larger the large-scale forcing (cooling/moistening), the larger the net condensation (heating/drying). They hypothesized that the effect of cloud microphysics is simply a response to the "imposed large-scale forcing in temperature and water vapor". The sensible heat flux is two to three orders of magnitude smaller than net condensation and large-scale forcing. The latent heat flux is about 17% and 5%, respectively, of large-scale forcing in the May and June cases. Net radiation results in cooling and is about 34% and 25%, respectively, of the net

condensation for the May and June cases. This result clearly suggests that radiation plays an important role in the precipitation processes for both cases.

There are several differences between the May and June cases. The first one is that the contribution by radiation and latent heat fluxes to precipitation is larger in the May case. The mean sea surface temperature is quite similar between May and June (27.99 C vs 28.2 C). However, the large-scale advective forcing in water vapor is very large in the lower troposphere and generates a moist boundary layer in June [Fig. 2(b)]. This reduces the contribution from latent heat fluxes from the ocean in the June case. The smaller large-scale temperature forcing in the May case is the reason for the larger contribution from radiation. Another difference is that net condensation is smaller than the large-scale water vapor forcing in the June case but not in the May case. Also, model results show a cold, dry bias for the May case and a warm, moist bias for the June case.

It is known that temperature and water vapor are closely related. Evaporative cooling/condensational heating is a source/sink for the water vapor field. On the other hand, latent heat flux from the ocean surface can provide water vapor for condensation heating. The moist static energy budget (Table 6) provides some additional information on the physical processes for both SCSMEX cases. The microphysical processes in the moist static energy budget are melting (cooling), freezing (heating) and, the product between the latent heat of fusion and the net deposition (deposition subtract sublimation)[3] (Eq. 7). These microphysical processes and the sensible heat fluxes are the smallest terms in the moist static energy budget. The local change term is negative for the May case but positive in the June case. Both the temperature and moisture bias contribute to a large positive value for the June case (see Tables 4 and 5). The large-scale advective forcing is larger (smaller) than the radiational cooling for the June (May) case. This effect contributes to a positive (negative) local change term in the June (May) case. For May, the negative local change in moist static energy is mainly from temperature (through radiation) not moisture. For June, the positive bias is from the large-scale water vapor forcing. The relationships between latent heat fluxes and the local change term are the opposite between the May and June case.

5. Sensitivity Tests

5.1 Cloud-Radiation Interaction

A sensitivity test is performed to examine the impact of cloud-radiation interaction on

---

[3] This term is usually positive that is to release heating in the model simulation (Fig. 15).

precipitation processes. In the test, the horizontal domain-averaged cloud fields are used to calculate cloud optical properties. Then, the radiative heating/cooling is applied horizontally uniform as with the imposed large-scale advective forcing. In this way, any inhomogeneities associated with cloud-radiation are eliminated, and the test can be interpreted as a large-scale cloud-radiation interaction case.

The model results indicate that cloud organization as well as stratiform rain percentage (Tables 2 and 6) does not change much in the sensitivity test compared to the control run for both the May and June case. The large-scale mean u-wind is the same between the sensitivity test and the control run. This explains why the different treatment for cloud-radiation interaction does not significantly impact convective organization. However, surface rainfall is reduced 7.5% and 8.8%, respectively, compared to the control runs for the May and June cases (Tables 2 and 6). The temperature and water vapor budgets for the sensitivity runs reveal that net radiative cooling is reduced by 8.8% and 11% with respect to net condensation, compared to the control runs for May and June, respectively.

Figure 16 shows the time- and domain-averaged shortwave heating and longwave cooling profiles for both the control runs and the sensitivity tests. Both longwave cooling and shortwave heating are reduced in the lower and upper troposphere in the sensitivity runs compared to the control runs for both the May and June cases. Net radiative cooling in the lower troposphere is slightly reduced by about 0.2 C day^{-1} in the sensitivity runs. The average large-scale advective cooling in the lower troposphere is about 2-3 C day^{-1} (Fig. 2). A 10% reduction in net condensation and rainfall in the sensitivity tests is consistent with the reduction in net radiative cooling. Latent heat fluxes are also reduced in the sensitivity runs but by less than 2% with respect to net condensation. Therefore, the reduction in net radiative cooling is the main physical process responsible for the reduction in rainfall. This is in good agreement with Tao *et al.* (1996) and some other previous cloud-resolving modeling results. Please see Tao (2002) for reviews and discussions on using cloud-resolving models to examine the impact of radiative cooling on the organization, structure and precipitation of convective systems.

5.2 *Microphysical Processes*

(a) Warm Rain Processes

The importance of ice microphysics to precipitation formation has long been known (please see a brief review in McCumber *et al.* 1991). The importance of ice microphysics to the formation of

stratiform rain has been identified in previous cloud modeling studies (Fovell and Ogura 1988; Tao and Simpson 1989; and others). A no-ice phase version of the GCE model, with a Kessler-type of two-category liquid water microphysics, is used to simulate the SCSMEX cases. One of major differences between the ice runs and the ice-free runs is that heavier precipitation accounts for a larger portion of the total rain in the ice-free runs. Only 42% and 28% of the rain is characterized as stratiform for the May and June cases respectively (Table 6). This is a reduction of 6 to 10% compared to the control runs. Another major difference is that less (16.5 to 18% reduction) total rain is produced in the ice-free runs (Tables 2 and 6). These results are consistent with previous modeling studies (i.e., Fovell and Ogura 1988; Tao and Simpson 1989; McCumber *et al.* 1991). Also, is found that the contribution by eddy heat flux convergence/divergence in the Q_1 budget is very small and can be neglected at middle levels in the ice-free runs. This is because the localized cooling/heating by the melting/freezing process is not allowed in the no-ice runs.

The temperature and water vapor budgets for the sensitivity runs reveal that net radiative cooling is reduced to 0 and -0.14 W m^{-2} for May and June, respectively. The cloud water is assumed to be monodisperse and to advect with airflow, having no appreciable terminal velocity of its own. Consequently, thick anvil clouds are simulated in the ice-free runs (Fig. 17). For high, thick anvil clouds, the effects on solar heating and long wave cooling are both large and largely offset each other (solar reflection is large, and long wave emission is low). As discussed in previous sensitivity tests, the reduction in net radiative cooling can decrease the net condensation and rainfall production. Also latent heat fluxes are reduced and that is because a warmer and more humid boundary layer compared to the control runs is simulated. That is caused by less net condensation (condensation subtract evaporation) in the boundary layer while large-scale advective forcing in water vapor still supplies abundant moisture.

(b) Ice Modification

Recently, the conversion of cloud ice to snow in the Goddard 3ICE schemes was modified (see Tao *et al.* 2002). An important process in the budget for cloud ice is the conversion of cloud ice to snow as the ice crystals grow by vapor deposition in the presence of cloud water, usually referred to as the Bergeron process and designated PSFI (production of snow from ice) by Lin et al. (1983). As described in Tao *et al.* (2002), the formulation generally used in the parameterization is independent of relative humidity, which causes ice to be converted to snow even when the air is sub-saturated with respect to ice. Two alternative formulations are proposed. In the first, the original formula is simply multiplied by an empirically derived relative-humidity dependency factor so that PSFI diminishes as the relative humidity approaches the ice saturation value. The second alternative

formulation is derived directly from the equation for depositional growth of cloud ice (Rutledge and Hobbs 1984) used in the model. This formulation causes PSFI to diminish as the relative humidity approaches the ice saturation value, but also ensures physical consistency with the parameterization of depositional growth of cloud ice used in the model. The two alternative formulations produce relatively similar results since simulated ice clouds over the tropical oceans often have vapor mixing ratios near the ice saturation value so that PSFI is very small. Another modification is the accretion of snow by graupel. This conversion process will be reduced under the presence of liquid water. This modification can reduce unrealistic abundant graupel in the stratiform region.

Figure 18 shows the simulated domain- and time-averaged cloud ice, snow and graupel for the June case using the original [Figs. 18(a), 18(b) and 18(c)] and the modified three-ice scheme [Figs. 18(d), 18(e) and 18(f)]. The main differences are an increase in cloud-top height and a substantial increase in the cloud ice mixing ratios, particularly at upper levels in the cloud, using the new formulation of PSFI. Another difference is a significant increase in snow and decrease in graupel in the new formulation of snow conversion to graupel. This increase in snow and decrease in graupel occurs in the stratiform region. Similar results are also found for the May case.

The model results indicate that cloud organization and stratiform rain percentage (Tables 2 and 6) are not affected very much due to the change in the microphysics. Again, this is because the same large-scale mean u-wind is imposed for the sensitivity tests and control runs. The surface rainfall, however, is reduced 5.7% and 4.4% respectively, compared to the control runs in the May and June cases (Tables 2 and 6). The temperature and water vapor budgets for the sensitivity runs indicate that longwave radiative cooling is reduced by 16% and 11% with respect to net condensation, compared to the control runs for May and June, respectively. Shortwave radiative heating is not altered by the different microphysical scheme, however. The higher cloud tops in the new PSFI formulation affect the longwave radiation much more than the shortwave radiation. Latent heat fluxes are only slightly reduced (less than 0.5%) with respect to net condensation in the sensitivity runs. The reduction in longwave radiative cooling is the main physical process responsible for the reduction in rainfall.

5.3 *Wind Shear*

The final sensitivity test addresses the impact of the mean wind-shear profile on precipitation processes. In the sensitivity test, the horizontal wind components, U and V, are set their respective surface values and held constant with height. U and V are allowed to change with time as

observed using the same nudging method in the control run. The results indicate that cloud organization (Fig. 19) as well as stratiform rain percentage at the surface (Table 6) is effected for both the May and June cases. Clouds and cloud systems in the sensitivity tests are less organized compared to the control runs.

However, surface rainfall and the individual terms in the temperature and water vapor budgets only change slightly (less than 1%). Using the same horizontal winds at the surface in the sensitivity tests is the main reason for the small difference in the surface fluxes between the sensitivity tests and the control runs. The thermodynamic structure of the boundary layer does not change significantly as the same large-scale advective forcing in temperature and water vapor is applied to both the sensitivity tests and the control runs. The domain- and time-average hydrometeor contents do not change between the sensitivity tests and control runs (not shown). Consequently, the radiation and Q_1 and Q_2 budgets do not change in the sensitivity tests. Similar results were obtained for a three-dimensional model simulation (Tao and Soong 1986). However, this might not be the case in the real atmosphere, since the large-scale advective forcing might be effected significantly when there is no large-scale environmental wind shear. Other cloud-resolving model simulations using the "self-forced convection" approach have shown that initial wind profiles can strongly influence the dynamics and rainfall predictions of model clouds (e.g., Cotton and Tripoli 1978; Wilhelmson and Klemp 1978 and many others). The use of the "continuous large-scale forced convection" approach prohibits the study of wind shear effects on precipitation prediction.

6. Comparison with TOGA COARE, GATE and ARM simulations

The GCE model has been used to simulate active convective events during TOGA COARE, GATE and ARM (Das *et al.* 1997; Tao *et al.* 1998; Johnson *et al.* 2002; Xu *et al.* 2002)[4]. The most intense convection during TOGA COARE occurred in middle and late December 1992. Westerlies started to appear near the surface over the TOGA COARE IFA in early December and gradually developed and intensified, although the middle and upper troposphere were still dominated by easterlies. The moderate vertical wind shear favored organized deep convection. Several major convective events occurred between 11-16 and 20-25 December 1992, mainly due to low-level large-scale convergence of easterlies and westerlies. However, synoptic conditions were different between the two periods. Easterly flow prevailed at low levels from near the date line westward to the IFA, and convection over the IFA arrived from the east with an easterly surge on 11-16 December. During

[4] This period has also been used by the GCSS working group 4 (WG4) model intercomparison project for CRMs and SCMs.

21-24 December, there was a greater contribution to heating from stratiform precipitation caused by the increased wind shear [see Lin and Johnson (1996)]. There was less of a stratiform contribution for the December 11-16 convective episode. Two periods, 10-17 December and 19-27 December 1992, have been simulated using the GCE model (Tao *et al.* 2000 and Johnson *et al.* 2002).

Cloud systems (nonsquall clusters, a squall line, and scattered convection) for the period of 1-7 September 1974 phase III of the Global Atmospheric Research Programme (GARP) Atlantic Experiment (GATE) were also simulated using the GCE model. The large-scale environments associated with the organized cloud systems that occurred in TOGA COARE and GATE were quite different. The large-scale advective forcing in temperature and water vapor as well as the large-scale vertical velocity are stronger for TOGA COARE than for GATE. The mean CAPE is larger in GATE than in TOGA COARE. The SST is higher for TOGA COARE (about 29 C vs 27.4 C for GATE). The vertically integrated water vapor content (precipitable water) is much drier for GATE (2.47 g cm-2) than TOGA COARE (5.15 g cm-2).

The ARM Summer 1997 Intensive Observing Period (IOP) at the Southern Great Plains (SGP) ARM Cloud and Radiation Testbed (CART) site in northern Oklahoma (DOE, 1996) covers a 29-day period from 18 June to 17 July. Three subperiods, 26-30 June, 7-12 July and 12-17 July 1997, are simulated using the GCE model. Details of the ARM IOP observations can be found in Ghan et al. (2000) and Xie et al. (2001). One major difference between the ARM simulations and the SCSMEX, TOGA COARE and GATE simulations is that interactive cloud-radiation and air-sea processes are not allowed in the ARM runs. Radiative heating rate profiles based on the European Center for Medium-range Weather Forecasting (ECMWF) that are adjusted by the observed column radiative fluxes and observed surface turbulent (latent and sensible) heat fluxes from Energy Balance/Bowen Ratio (EBBR) measurements are imposed. See Xu *et al.* (2002) for more details on the ARM cases.

Tables 7, 8 and 9 show temperature, water vapor and moist static energy budgets. Large-scale advective forcing in temperature and water vapor is largest in the TOGA COARE cases. Consequently, net condensation is also the largest in TOGA COARE. Large-scale forcing and surface latent heat fluxes are approximately an order of magnitude larger than the other processes in the moist static energy budget. Net radiation is very small and does not contribute to the total net condensation (precipitation processes) for TOGA COARE cases. This is because thick anvil clouds are simulated in the TOGA COARE cases. However, the radiation process still plays an important role in diurnal variability of rainfall.

For GATE, latent heat flux and net radiation play an important role in the water vapor and

temperature budget, respectively. This agrees with the May SCSMEX results but not the June ones. Latent heat flux is an order of magnitude smaller than both large-scale forcing and net condensation in the water vapor budget for the SCSMEX June case. Interestingly, the large-scale forcing in the moist static energy budget is negative (large-scale cooling exceeds large-scale moistening) for the TOGA COARE and GATE cases. For SCSMEX, however, there is more large-scale moistening than cooling. This suggests that the imposed large-scale advective forcing in water vapor is quite important for convective processes in the SCSMEX cases.

Net radiation and sensible heat and latent heat fluxes play a much more important role in the three ARM cases than those in the tropical cases (Tables 7 and 8). Latent heat fluxes are much larger than the large-scale forcing in the water vapor budget for the two July cases (relatively weak convective events compared to other cases). They contribute 76% and 90% of net condensation for two July cases, respectively. They are the main source of moisture for condensation. This means the accurate measurement of surface fluxes is crucial for simulating the ARM cases. However, the budget for the ARM June case is quite different from the two July cases. First, the large-scale water vapor forcing is important and contributes about 65% of the net condensation (Table 8). Second, the large-scale water vapor forcing is stronger than the large-scale temperature forcing in the June case (Table 9).

The total precipitation efficiency (PE) in the simulations can be defined as the ratio of the total rainfall to the total condensation (condensation onto water plus deposition onto ice for all hydrometeor species). A similar definition of precipitation efficiency was adopted in the three-dimensional modeling study of Weisman and Klemp (1982), in which precipitation efficiencies varied from 11 to 49 percent over the 2-h duration of their simulations. Ferrier *et al.* (1996) investigated the precipitation efficiency of convective systems under widely varying large-scale conditions using the GCE model. Their results indicated that the vertical orientation of the updrafts, which is controlled by the vertical wind shear, and the ambient moisture content are important in determining precipitation efficiency. However, these modeling studies only examined the PE associated with individual clouds or cloud systems, not ensembles of clouds/cloud systems.

The total precipitation efficiency (PE) ranges from 32% to 45% in the GCE-simulated SCSMEX, TOGA COARE, GATE and ARM cases (Table 10). The two SCSMEX cases have very similar PEs (45.4 and 45.3%) and are the largest among all the simulations. This result suggests that the larger vertical u-wind shear in the SCSMEX June case does not produce larger precipitation efficiency. However, TOGA COARE 1 (December 19-26) has a larger PE as well as stronger wind shear than TOGA COARE 2 (December 10-17). It may be expected that the ARM

(midlatitude and continental) and GATE cases would have lower PEs because they developed under drier environments. One of the ARM July cases has the smallest PE (32%), but the GATE and the June ARM cases have relatively large PEs, 44.5% and 40.1%, respectively. No definite relationship between the PE and wind shear, and the large-scale environment is found in these cloud ensemble model simulations. It is also found that there is no clear relationship between the PE and rainfall, the net condensation, or the large-scale forcing (Tables 3,4, 7, 8 and 10). However, the model results show that the two SCSMEX cases and the GATE case have large, positive net condensation in the moist static energy budget, and they all have larger PEs. One of the ARM June cases and one of the TOGA COARE cases have negative net condensation as well as small PE. A positive net condensation in the moist static energy budget indicates that there is net melting (melting subtract freezing) and/or net deposition (deposition subtract sublimation).

The rainfall amount simulated by the GCE model and estimated by soundings is in excellent agreement (within 0.5%) with each other for both TOGA COARE cases (i.e., see Johnson *et al.* 2002). The model underestimates the rainfall by 10% for the GATE case. For the ARM cases, however, the GCE model underestimates rainfall by about 10% in the June case and overestimate rainfall by 16% and 10%, respectively, for the two July cases[5]. All of these cases are forced by a prescribed large-scale advective forcing determined from soundings. The radiation and surface fluxes can be influenced by clouds simulated by the models and may cause the rainfall differences between the model and the sounding estimates. For the ARM cases, the radiation and surface fluxes are prescribed, but not for the SCSMEX, GATE and TOGA COARE cases. Based on the moist static energy budget, the GCE can underestimate (overestimate) the rainfall when a positive (negative) large-scale forcing is imposed/prescribed (except for the GATE case). This result may imply that the GCE model could underestimate the rainfall (when compared to sounding estimates) when the large-scale advective water vapor forcing exceeds the large-scale temperature forcing. More thorough cloud ensemble modeling studies will be needed to generalize this relationship as well as the relationship between PE and net condensation in the moist static energy budget.

7. Summary and Conclusions

The two-dimensional version of the GCE model has been used to simulate two SCSMEX convective periods [May 18-26 (prior to and during the monsoon) and June 2-11 (after the onset of the monsoon), 1998]. Observed large-scale advective tendencies (or forcing) of potential temperature, water vapor mixing ratio, and horizontal momentum (Johnson and Ciesielski 2002) are used as the main

---

[5] Similar errors have been found with other cloud-resolving models in simulating ARM cases (see Table 9 in Xu *et al.* 2002).

forcing in governing the GCE model in a semi-prognostic manner (Soong and Tao1980; Tao and Soong 1986; and many others). The SCSMEX June case has stronger forcing in both temperature and water vapor. In addition, there is stronger low-level vertical shear in the u-wind component and a larger CAPE during the June period.

The major results can be summarized as follows:

- The GCE-model results captured many of the observed precipitation characteristics. For example, the model simulated rainfall temporal variation compared quite well to the sounding-estimated rainfall. However, the model underestimates the rainfall by 17 to 20% compared to that calculated based on soundings. The GCE-model-simulated rainfall for June is in very good agreement with the TRMM PR and GPCP, but not the TMI. Also, a single peaked rainfall probability distribution is well simulated by the model for the June case. But an observed bimodal rainfall distribution in May case is not captured by the model.
- Both unicell and multi-cell types of convective systems are simulated by the model. They are determined by the observed mean U-wind shear (uni-directional or reverse shear profiles above midlevel). Both types of convective systems can contribute large amounts of rainfall and associated latent heating. Cloud-cloud interactions and mergers is also a common feature in the model simulations.
- The time- and domain-averaged heating and moisture budgets are generally in good agreement with those diagnostically determined from soundings. However, model results show more temporal variability. Overall, the model agrees better with observations in the June case than in the May case.
- The net condensation (condensation, evaporation, deposition and sublimation, melting and freezing) and the large-scale temperature forcing are the largest terms and are opposite in sign in the Q_1 budget in both cases. The contribution by eddy heat flux convergence/divergence in the Q_1 budget can not be neglected at middle levels. This feature is related to localized cooling by the melting process. Net radiation results in cooling, and it contributes about 30% of the net condensation. The June case has larger net condensation because it has stronger large-scale advective forcing in temperature.
- The model results also indicated that the net condensation and the imposed large-scale advective water vapor forcing are opposite in sign in the Q_2 budget. The net vertical eddy convergence/divergence of moisture by clouds is quite important for the Q_2 budget. The larger contribution by vertical eddy convergence/divergence in the Q_2 budget is the main reason for Q_1 and Q_2 de-coupling.
- The model results show that more stratiform rain is simulated in the May case than the

June case. The smaller large-scale advective forcing in temperature and water vapor, and the U-wind shear profile for the May case produce more light precipitation that is categorized as stratiform than in the June case. The typical convective and stratiform Q_1 and Q_2 structures (or shapes) discussed in Houze (1997) and Johnson (1984) are captured by the model for both cases.

- The surface energy budgets are calculated and results show that there are more latent heat fluxes prior to the onset of the monsoon (May case). The sensible heat fluxes does not contribute to precipitation processes in either SCSMEX case. Also, the results indicate that there is more large-scale advective forcing in water vapor (moistening) than temperature (cooling). This suggests that the imposed large-scale advective forcing in water vapor is very important for convective processes in the SCSMEX cases.
- Several sensitivity tests are performed to examine the impact of the radiation, microphysics and large-scale mean horizontal wind on the organization and intensity of the SCSMEX convective systems. Total rain production is reduced by about 17-18% in the ice-free runs. The model results are also sensitive to ice processes and cloud-radiation interaction. The large-scale mean horizontal wind can play an important role in the organization of the cloud systems but not the precipitation processes.
- The same GCE model has simulated convective systems that developed during other field campaigns (i.e., TOGA COARE, GATE and ARM), and those results are compared with the ones from SCSMEX. Large-scale advective forcing in temperature and water vapor are the major energy sources for net condensation in the tropical cases. The large-scale cooling exceeds large-scale moistening for the TOGA COARE and GATE cases. For SCSMEX, however, there is more large-scale moistening than cooling. However, net radiation and the sensible and latent heat fluxes play a much more important role in the three ARM cases. Latent heat fluxes contribute 76% and 90% of the net condensation for the two ARM July cases.
- The model results suggest that cases with large, positive net condensation in the moist static energy budget tend to have a large precipitation efficiency (PE) usually has a. The model results also suggest that the GCE can underestimate (overestimate) the rainfall when a positive (negative) large-scale forcing is imposed/prescribed (except for the GATE case). More thorough cloud ensemble modeling studies will be needed to generalize these relationships.

Real clouds and cloud systems are three-dimensional. Because of the limitations of computer resources, however, most cloud ensemble models (CEMs) today are still two-dimensional (Krueger 1988; Xu 1995; Xu and Randall 1996; Tao *et al* 1996; and many others; see a review by

Johnson *et al.* 2002). Few 3-D CEMs (e.g., Tao and Soong 1986; Tao *et al.* 1987; Lipps and Hemler 1986) have been used to study the response of clouds to large-scale forcing. The 3-D GCE modeling results, however, are in better agreement with the aircraft measured updrafts and downdrafts (Zipser and LeMone 1980) in the middle troposphere. In addition, the 2-D and 3-D simulations differed between 2% (in the lower troposphere) and 10% (between 300 and 400 mb) in fractional cloud coverage. In these 3-D simulations, the model domain was small and integration times were between 3 and 6 hours. Only recently, 3-D experiments were performed for multi-day periods for tropical cloud systems with large horizontal domains (500 by 500 km^2) at the National Center for Atmospheric Research (Wu *et al.* 1998; Grabowski *et al.* 1998), at NOAA/GFDL (Donner *et al.* 1999), at Colorado State University (Khairoutdinov, see Xu *et al.* 2002) and at NASA/Goddard Space Flight Center (Tao 2002). At Goddard, a 3-D GCE model was used to simulate periods during TOGA COARE (December 19-27, 1992) and GATE (September 1-7, 1974) using a 512 by 512 km domain (with 2 km resolution). The preliminary results indicate that cloud statistics as well as surface precipitation and latent heating profiles are very similar to the 2-D GCE model simulations. Grabowski *et al.* (1998) also found a similar conclusion for their GATE and TOGA COARE multi-day 2-D and 3-D simulations. The reason for the strong similarity between the 2-D and 3-D CEM simulations is that the same observed (time-varying) large-scale advective tendencies of potential temperature, water vapor mixing ratio, and horizontal momentum were used as the main forcing in both the 2-D and 3-D models. However, it was found that the 3-D GCE modeled water vapor (Q_2) budget is in better agreement with observations in the lower troposphere than its 2-D counterpart. We are in the process of using the 3-D GCE model to simulate the SCSMEX cases and ARM cases and will report our results in a publication in the near future.

8. Acknowledgements

This work is mainly supported by the NASA Headquarters Atmospheric Dynamics and Thermodynamics Program and the NASA Tropical Rainfall Measuring Mission (TRMM). The authors are grateful to Dr. R. Kakar at NASA headquarters for his support of this research. The authors thank Mr. S. Lang for reading the manuscript.

Acknowledgment is also made to the NASA/Goddard Space Flight Center for computer time used in this research.

9. References

Adler, R. F., H.-Y. Yeh, N. Prasad, W.-K. Tao and J. Simpson, 1991: Microwave rainfall

simulations of a tropical convective system with a three-dimensional cloud model. *J. Appl. Meteor.*, 30, 924-953.

Chong, M., and D. Hauser, 1990: A tropical squall line observed during the COPT 81 experiment in West Africa. Part III: Heat and moisture budgets. *Mon. Wea. Rev.*, 118, 1696-1706.

Chin, H.-N. S., 1994: The impact of the ice phase and radiation on a mid-latitude squall line system. *J. Atmos. Sci.* 51, 3320-3343.

Churchill, D. D., and R. A. Houze, Jr., 1984: Development and structure of winter monsoon cloud clusters on 10 December 1978. *J. Atmos. Sci.*, 41, 933-960.

Cotton, W. R. and G. J. Tripoli, 1978: Cumulus convection in shear flow - three-dimensional numerical experiments. *J. Atmos. Sci.*, 35, 1053-1521.

Das, S., D. Johnson and W.-K. Tao, 1999: Single-column and cloud ensemble model simulations of TOGA COARE convective systems, *J. Meteor. Soc. Japan*, 77, 803-826.

Deardorff, J. W., 1975: The development of boundary-layer turbulence models for use in studying the severe storm environment. *Proceedings of the SESAME Opening Meeting*, Boulder, NOAA-ERL, 251-264.

Dudhia, J., M. W. Moncrieff and D. W. K. So, 1987: The two-dimensional dynamics of West African squall lines. *Q. J. R. Meteorol. Soc.*, 113, 121-146.

Ferrier, B. S., 1994: A double-moment multiple-phase four-class bulk ice parameterization. Part I: Description. *J. Atmos. Sci.*, 51, 249-280.

Ferrier, B.S., W.-K. Tao and J. Simpson,1995: A double-moment multiple-phase four-class bulk ice scheme. Part II: Simulations of convective storms in different large-scale environments and comparisons with other bulk parameterizations. *J. Atmos Sci.*, 52, 1001-1033.

Fovell, R. G., and Y. Ogura, 1988: Numerical simulation of a midlatitude squall line in two dimensions. *J. Atmos Sci.*, **45**, 3846-3879.

Frank, W. M., H. Wang, and J. L. McBride, 1996: Rawinsonde budget analysis during the TOGA COARE IOP. *J. Atmos. Sci.*, 53, 1761-1780.

Gallus, W. A., Jr. and R. H. Johnson, 1991: Heat and moisture budgets of an intense midlatitude squall line. *J. Atmos. Sci.*, 48, 122-146.

Grabowski, W. W., X. Wu, M. W. Moncrieff, and W. D. Hall, 1998: Cloud-resolving modeling of cloud systems during Phase III of GATE. Part II: Effects of resolution and the third spatial dimension. *J. Atmos. Sci.*, 55, 3264- 3282.

Halverson, J. R., B. S. Ferrier, J. Simpson and W.-K. Tao, 1996: Two-dimensional numerical modeling investigations of the February 11, 1993 TOGA COARE mesoscale convective system. *AMS 7th Conf. Mesoscale Processes*, Reading, U.K. 165-167.

Houze, R. A., Jr., 1982: Cloud clusters and large-scale vertical motions in the tropics. *J. Meteor. Soc. Japan*, 60, 396-409.

Houze, R. A., Jr., 1989: Observed structure of mesoscale convective systems and implications for large-scale heating. *Quart. J. Roy. Meteor. Soc.*, 115, 425-461.

Houze, R. A., Jr., 1997: Stratiform precipitation in regions of convection: A meteorological paradox. *Bull. Amer. Meteor. Soc.*, 78, 2179-2196.

Johnson, R. H., 1984: Partitioning tropical heat and moisture budgets into cumulus and mesoscale components: Implication for cumulus parameterization. *Mon. Wea. Rev.*, 112, 1656-1665.

Johnson, R. H., and P. E. Ciesielski, 2000: Rainfall and radiative heating estimates from TOGA COARE atmospheric budgets. *J. Atmos. Sci.*, 57, 1497-1514.

Johnson, R. H., and P. E. Ciesielski, 2002: Characteristics of the 1998 Summer monsoon onset over the Northern South China Sea. *J. Metro. Soc. Japan*, (submitted).

Johnson, D., W.-K. Tao, J. Simpson, and C.-H. Sui, 2002: A study of the response of deep tropical clouds to large-scale processes, Part I: Model set-up strategy and comparison with observation, *J. Atmos. Sci.*. (accepted).

Klemp, J. B., and R. Wilhelmson, 1978: The simulation of three-dimensional convective storm dynamics. *J. Atmos. Sci.*, 35, 1070-1096.

Krueger, S. K., 1988: Numerical simulation of tropical cumulus clouds and their interaction with the subcloud layer. *J. Atmos. Sci.*, 45, 2221-2250.

Kummerow, C., W. S. Olson, and L. Giglio, 1996: A simplified scheme for obtaining precipitation and vertical hydrometeor profiles from passive microwave sensors. *IEEE Trans. Geosci. Remote Sensing*, 34, 1213-1232.

Lau, K. M., Y. Ding, J.-T. Wang, R. Johnson, T. Keenan, R. Cifelli, J. Geriach, O. Thiele, T. Rickenbach, S.-C. Tsay, and P.-H. Lin, 2000: A report of the field operations and early results of the South China Sea Monsoon experiment (SCSMEX). *Bull. Amer. Meteor. Soc.*, 81, 1261-1270.

Lin, Y.-L., R. D. Farley and H. D. Orville, 1983: Bulk parameterization of the snow field in a cloud model. *J. Clim. Appl. Meteor.*, 22, 1065-1092.

Lin, X., and R. H. Johnson, 1996: Heating, moistening and rainfall over the western Pacific during TOGA COARE. *J. Atmos. Sci.*, 53, 3367-3383.

Lipps, F. B., and R. S. Hemler, 1986: Numerical simulation of deep tropical convection associated with large-scale convergence. *J. Atmos. Sci.*, 43, 1796-1816.

Lynn, B. H., W.-K. Tao and P. Wetzel, 1998: A study of landscape generated deep moist convection. *Mon. Wea. Rev.*, 126, 928-942.

Mapes, B. E., and R. A. Houze, Jr., 1995: Diabatic divergence profiles in Western Pacific Mesoscale Convective Systems. *J. Atmos. Sci.*, 52, 1807-1828.

Moncrieff, M. W., S. K. Krueger, D. Gregory, J.-L. Redelsperger and W.-K. Tao, 1997: GEWEX Cloud System Study (GCSS) Working Group 4: Precipitating convective cloud systems. *Bull. Amer. Meteor. Soc.*, 78, 831-845.

Olson, W. S., C. D. Kummerow, G. M. Heymsfield, and L. Giglio, 1996: A method for combined passive-active microwave retrievals of cloud and precipitation profiles. *J. Appl. Meteor.*, 35, 1763-1789.

Olson, W. S., C. D. Kummerow, Y. Hong, and W.-K. Tao, 1999: Atmospheric latent heating distributions in the Tropics derived from passive microwave radiometer measurements. *J. Appl. Meteor.*, 38, 633-664.

Prasad, N, H.-Y. M. Yeh, R. F. Adler and W.-K. Tao, 1995: Infrared and microwave simulations of an intense convective system and comparison with aircraft observations. *J. Appl Meteor.*, 34, 153-174.

Redelsperger, J. L., P. R. A. Brown, F. Guichard, C. Hoff, M. Kawasima, S. Lang, Th. Montmerle, K. Nakamura, K. Saito, C. Seman, W.-K. Tao and L. J. Donner, 1999: A GCSS model intercomparison for a tropical squall line observed during TOGA-COARE. Part 1: Cloud-Resolving Models. *Q. J. R. Met. Soc.*, (in press).

Rickenback, T. M., and Coauthors, 1998: Monsoon convection during the South China Sea Monsoon Experiment observed from shipboard and the TRMM satellite. Preprint, 23rd *Conf. On Hurricanes and Tropical Meteorology*, Amer. Meteor. Soc., Dallas, TX, 943-945.

Rutledge, S.A., and P.V. Hobbs, 1984: The mesoscale and microscale structure and organization of clouds and precipitation in midlatitude clouds. Part XII: A diagnostic modeling study of precipitation development in narrow cold frontal rainbands. *J. Atmos. Sci.*, 41, 2949-2972.

Simpson, J. and W.-K. Tao, 1993: The Goddard Cumulus Ensemble Model. Part II: Applications for studying cloud precipitatiing processes and for NASA TRMM. *Terrestrial ,Atmospheric and Oceanic Sciences*, 4, 55-96.

Simpson, J., R. F. Adler, and G. R. North, 1988: A proposed satellite tropical rainfall measuring mission (TRMM). *Bull. Amer. Meteor. Soc.*, 69, 278-295.

Simpson, J., C. Kummerow, W.-K. Tao and R. Adler, 1996: On the Tropical Rainfall Measuring Mission (TRMM) *Meteor, and Atmos. Phys.* 60, 19-36.

Soong, S.-T., and Y. Ogura, 1980: Response of tradewind cumuli to large-scale processes. *J. Atmos. Sci.*, 37, 2035-2050.

Soong, S.-T., and W.-K. Tao, 1980: Response of deep tropical clouds to mesoscale processes. *J. Atmos. Sci.*, 37, 2016-2036.

Steiner, M. R., R. A. Houze, Jr. and S. E. Yuter, 1995: Climatological characterization of three-dimensional storm structure from operational radar and rain gauge data. *J. Appl. Meteor.*, 34, 1978-2007.

Sui, C.-H., and K.-M. Lau 1989: Origin of low-frequency (Intraseasonal) oscillations in the tropical atmosphere. Part II: Structure and propagation of mobile wave-CISK modes and their modification by lower boundary forcings. *J. Atmos. Sci.*, 46, 37-56.

Tao, W.-K., and J. Simpson, 1984: Cloud interactions and merging: Numerical simulations. *J. Atmos. Sci.*, 41, 2901-2917.

Tao, W.-K., and S.-T. Soong, 1986: A study of the response of deep tropical clouds to mesoscale processes: Three-dimensional numerical experiments. *J. Atmos. Sci.*, 43, 2653-2676.

Tao, W.-K., J. Simpson, and S.-T. Soong, 1987: Statistical properties of a cloud ensemble: A numerical study. *J. Atmos. Sci.*, 44, 3175-3187.

Tao, W.-K., and J. Simpson, 1989: Modeling study of a tropical squall-type convective line. *J. Atmos. Sci.*, 46, 177-202.

Tao, W.-K., and J. Simpson, 1993: The Goddard Cumulus Ensemble Model. Part I: Model description. *Terrestrial,Atmospheric and Oceanic Sciences*, 4, 19-54.

Tao, W.-K., J. Simpson, S. Lang, M. McCumber, R. Adler and R. Penc, 1990: An algorithm to estimate the heating budget from vertical hydrometeor profiles. *J. Appl. Meteor.*, 29, 1232-1244.

Tao, W.-K., S. Lang, J. Simpson and R. Adler, 1993a: Retrieval Algorithms for estimating the vertical profiles of latent heat release: Their applications for TRMM. *J. Meteor. Soc. Japan* , 71, 685-700.

Tao, W.-K., J. Simpson, C.-H. Sui, B. Ferrier, S. Lang, J. Scala, M.-D. Chou and K. Pickering, 1993b: Heating, moisture and water budgets of tropical and midlatitude squall lines: Comparisons and sensitivity to longwave radiation. *J. Atmos. Sci.*, 55, 673-690.

Tao, W.-K., J. Scala, and J. Simpson, 1995: The effects of melting processes on the development of a tropical and a mid-latitudes squall line. *J. Atmos. Sci.*, 52, 1934-1948.

Tao, W.-K., J. Simpson, S. Lang, C.-H. Sui, B. Ferrier, and M.-D. Chou, 1996: Mechanisms of cloud-radiation interaction in the tropics and midlatitudes. *J. Atmos. Sci* . 53, 2624-2651.

Tao, W.-K., J. Simpson and B. Ferrier, 1997: Cloud Resolving Model Simulations of Mesoscale Convective Systems. *New Insights and Approaches to Convective Parameterization* , Ed. D. Gregory, 77-112.

Tao, W.-K., S. Lang, J. Simpson, W. S. Olson, D. Johnson, B. Ferrier, C. Kummerow and R. Adler, 2000: Vertical profiles of latent heat release and their retrieval in TOGA COARE convective systems using a cloud resolving model, SSM/I and radar data, *J. Meteor. Soc. Japan*, 78, 333-355.

Tao, W.-K., J. Simpson, D. Baker, S. Braun, M.-D. Chou, D. Johnson, B. Ferrier, A. Khain, S. Lang, B. Lynn, C.-L. Shie, D. Starr, C.-H. Sui, Y. Wang and P. Wetzel, 2002: Microphysics, Radiation and Surface Processes in a Non-hydrostatic Model. *Meteorology and Atmospheric Physics* (in press).

Wang, Y., W.-K. Tao and J. Simpson, 1996: The impact of ocean surface fluxes on a TOGA COARE cloud system. *Mon. Wea. Rev.* 124, 2753-2763.

Webster, P. J., and R. Lukas, 1992: TOGA COARE: The Coupled Ocean-Atmosphere Response Experiment. *Bull. Amer. Meteor. Soc.*, 73, 1377-1416.

Wilhelmson, R. B., and J. B. Klemp, 1978: A numerical study of storm splitting that leads to long-lived storms. *J. Atmos. Sci.*, 35, 1975-1986.

Xu, K.-M., 1995: Partitioning mass, heat, and moisture budgets of explicit simulated cumulus ensembles into convective and stratiform components. *J. Atmos. Sci.*, 52, 551-573.

Xu, K.-M., and D. A. Randall, 1996: A semiemprical cloudiness parameterization for used in climate models. *J. Atmos. Sci.*, 53, 3084-3102.

Xu, K.-M., R. T. Cederwall, L. J. Donner, F. Guichard, W. W. Grabowski, D. E. Johnson, M. Khairoutdinov, S. K. Krueger, J. C. Petch, D. A. Randall, C. J. Seman, W.-K. Tao, S. Xie, J. Jio and M.-H. Zhang, 2002: Iintercomparison of cloud-resolving models with the ARM Summer 1997 IOP data *Q. J. R. Met. Soc.* (in press).

Yanai, M., S. Esbensen and J. Chu, 1973: Determination of average bulk properties of tropical cloud clusters from large-scale heat and moisture budgets *J. Atmos. Sci.*, 30, 611-627.

Yang, S., and E. A. Smith, 1999: Four dimensional structure of monthly latent heating derived from SSM/I satellite measurements. *J. of Climate*, (in press).

Yeh, H.-Y., M. N. Prasad, R. Meneghini, W.-K. Tao and R.F. Adler, 1995: Model-based simulation of TRMM spaceborne radar observations. *J. Appl Meteor.*, 34, 175-197.

Yuter, S. E., and R. A. Houze, Jr., 1995: Three-dimensional kinematic and microphysical evolution of Florida cumulonimbus. Part III: Vertical mass transport, mass divergence, and synthesis. *Mon. Wea. Rev.*, 123, 1964-1983.

FIGURE CAPTIONS

Fig. 1 Horizontally-averaged diagnosed large-scale advective forcing in **(a)** temperature (C day^{-1}) and **(b)** water vapor (C day^{-1}) for the 18-26 May 1998 period. **(c)** and **(d)** are the same as (a) and (b) expect for the 2-11 June 1998 period. The contour interval is 2 C day^{-1}.

Fig. 2 Time-averaged large-scale advective forcing in **(a)** temperature and **(b)** water vapor. The solid line is the 18-26 May 1998 period and the dashed line the 2-11 June 1998 period.

Fig. 3 Horizontally-averaged mean large-scale **(a)** u-wind (m s^{-1}), **(b)** v-wind (m s^{-1}), and **(c)** w-velocity (mb h^{-1}) for the 18-26 May 1998 period. The contour interval is 2 m s^{-1}, 2 m s^{-1}, and 1 mb h^{-1}) for (a), (b) and (c), respectively. **(d)**, **(e)** and **(f)** are the same as (a), (b) and (c) expect for the 2-11 June 1998 period.

Fig. 4 Time-averaged large-scale **(a)** u-, **(b)** v-, and **(c)** w-wind. The solid line is for the 18-26 May 1998 period and dashed line is for the 2-11 June period.

Fig. 5 Time sequence of the GCE model estimated domain mean surface rainfall rate (mm h^{-1}) for **(a)** the 18-26 May 1998 period and **(b)** the 2-11 June 1998 period.

Fig. 6 Vertical cross-sections of **(a)** the ice and liquid water content, **(b)** the equivalent potential temperature deviation, **(c)** the horizontal wind speed deviated from its horizontal mean and **(d)** the w-velocity after seven days of simulation for the June SCSMEX case. The contour interval is 1 g kg^{-1}, 2 K, 2 m s^{-1} and, 1 m s^{-1}, for (a), (b), (c) and (d), respectively. **(e)**, **(f)**, **(g)** and **(h)** are the same as (a), (b), (c) and (d), respectively, except for the May SCSMEX case after three days of simulation.

Fig. 7 Time-sequence of the GCE-model-estimated domain-mean surface rainfall rate (mm h^{-1}) for **(a)** May 18-26 and **(b)** June 2-11 1998. **(c)** and **(d)** are rainfall estimated using Q_2 budget.

Fig. 8 Probability distribution of simulated rainfall for the **(a)** May and **(b)** June SCSMEX cases. **(c)** and **(d)** are the same as (a) and (b) except for estimated rainfall by sounding.

Fig. 9 Evolution of the domain-average apparent heat source (Q_1) for SCSMEX for the 8-day period May 18-26, 1998. **(a)** Derived diagnostically from soundings (Johnson and

Ciesielski 2002) **(b)** Simulated from the GCE model. The GCE model simulated Q_1 over **(c)** the convective region and **(d)** the stratiform region. The contour interval is 4 C day^{-1} for (a), (b), (c) and (d).

Fig. 10 Same as Fig. 9 except for the June 2-11, 1998 period.

Fig. 11 Same as Fig. 9 except for the Q_2 budget.

Fig. 12 Same as Fig. 10 except for the Q_2 budget.

Fig. 13 Eight-day average profiles of **(a)** Q_1 (C day^{-1}) and **(c)** Q_2 (C day^{-1}) for the period May 18-26, 1998. GCE model simulated Q_1 for the convective and stratiform regions are shown as dashed and dotted lines, respectively. Diagnostically derived profiles are also shown. **(b)** and **(d)** are the same as (a) and (c) except for the nine-day period June 2-11, 1998.

Fig. 14 Heating **(a)** and moisture **(c)** budgets for the May SCSMEX case averaged over the 8-day simulation time. Contributions from net condensation (condensation+deposition-evaporation-sublimation, in thick solid line) and the total vertical eddy-flux convergence [includes both cloud-scale and sub-grid-scale (turbulence) effects, in thick dashed line] are shown. The imposed large-scale advective forcing (thin solid line) and net radiation (thin dashed line) are also shown. **(b)** and **(d)** are the same as (a) and (c), except for the June case.

Fig. 15 **(a)** Vertical profiles of domain- and time-average accumulated condensation (thick solid line), evaporation (thin solid line), deposition (thick dashed line), sublimation (thin dashed line), melting (thin dotted line) and freezing (thick dotted line) for the May SCSMEX case. **(b)** is the same as (a) except for the June case.

Fig. 16 Vertical profiles of time- and domain-average radiation (total, longwave cooling and shortwave heating) for the **(a)** May and **(b)** June SCSMEX cases. **(c)** and **(d)** are the same as (a) and (b) except for the sensitivity tests.

Fig. 17 Evolution of the domain-averaged **(a)** cloud water for the May SCSMEX case. **(b)** is the same as (a) except for the June case.

Fig. 18 Evolution of the domain-averaged **(a)** cloud ice, **(b)** snow and **(c)** graupel for the 9-day period June 2-11,1998. **(d)**, **(e)**, and **(f)** are the same as (a), (b) and (c) except for the microphysical sensitivity tests. The contour interval is 0.005, 0.005 and 0.02 g kg^{-1}, for (a), (b) and (c), respectively.

Fig. 19 Same as Fig. 5 except for the wind shear sensitivity tests.

TABLES

Table 1 Initial environmental conditions expressed in terms of CAPE (Convective Available Potential Energy), lifted index, precipitable water and Richardson number for the 18-26 May and 2-11 June 1998 periods.

Table 2 Domain-averaged surface rainfall amounts and stratiform percentage for both the May and June cases. Rainfall amounts and stratiform estimated by TRMM PR, TMI and sounging network are also shown.

Table 3 Temperature budgets for the 18-26 May and 2-11 June 1998 cases. Net condensation is the sum of condensation, deposition, evaporation, sublimation, freezing and melting of cloud. Large-scale forcing is the imposed large-scale advective effect on temperature, and $d(C_pT)$ is the local time change of temperature. Long wave cooling, short wave heating and their net radiative processes are shown in Q_R. Units are in W m^{-2}.

Table 4 Same as in Table 3 except for the water budgets. Net condensation is the sum of condensation, deposition, evaporation and sublimation of cloud. Large-scale forcing is the imposed large-scale advective effect on water vapor, and $L_v d(q_v)$ is the local time change of water vapor. Units are in W m^{-2}.

Table 5 Same as Table 4 except for the moist static energy budget.

Table 6 Same as Table 2 expect for the sensitivity tests.

Table 7 Same as Table 3 except for the TOGA COARE, GATE and ARM cases. TOGA COARE 1 and 2, respectively, is for December 19-27 and December 10-17, 1992 case. ARM A, B and C, respectively is for 26-30 June, 7-12 July and 12-17 July 1997 case.

Table 8 Same as Table 4 except for the TOGA COARE, GATE and ARM cases.

Table 9 Same as Table 5 except for the TOGA COARE, GATE and ARM cases.

Table 10 Precipitation efficiency (PE in %), domain-averaged surface rainfall amounts (in mm day^{-1}) and total net condensation (condensation plus deposition, in mm day^{-1}) for SCSMEX, TOGA COARE, GATE and ARM cases.

Table 1

	CAPE m^2s^{-2}	Lifted Index	Precipitable Water ($g\ cm^{-2}$)	Richardson Number
May18-May 26, 1998	825	-0.91	62.53	55.4
June 2 – June 11, 1998	1324	-1.92	62.34	100.28

Table 2

	GCE Rainfall /Stratifrom (%)	Sounding Rainfall	PR Rainfall /Stratifrom (%)	TMI Rainfall /Stratifrom (%)	GPCP Rainfall
May18-May 26 1998	11.14/49	13.00	10.56/33	24.22/26	14.22
June 2 – June 11, 1998	16.46/38	20.71	17.93/44	31.95/31	16.38

Table 3

	dT/dt	Net Condensation	Large-scale Forcing	Net Q_R=SW-LW	Sensible Heat Fluxes
May18 - May 26	-0.12	2.83	-2.03	-0.95=0.70-1.65	0.03
June 2 – June 11	0.26	4.17	-2.88	-1.04=0.69-1.73	0.01

Table 4

	d(Qv) /dt	Net Condensation	Large-scale Forcing	Latent Heat Fluxes
May18 - May 26	-0.15	-11.23	9.81	1.27
June 2 – June 11	1.12	-16.45	16.84	0.73

Table 5

	D(CpT+ LvQv)	Net Condensation	Large-scale Forcing	Net Q_R	Sensible Heat Fluxes	Latent Heat Fluxes
May18 - May 26	-18.0	2.84	48.8	-110.7	4.2	36.85
June 2 – June 11	62.4	3.55	156.6	-119.9	1.07	21.11

Table 6

	Uniform Radiation		Warm Rain		Modified 3-Ice Scheme		Uniform U-wind	
	Rainfall (mm/day)	Stratiform (%)	Rainfall (mm/day)	Stratiform (%)	Rainfall (mm/day)	Stratiform (%)	Rainfall (mm/day)	Stratiform (%)
May 18 – May 26	10.30	47	9.10	42	10.51	52	11.25	43
June 2 – June 11	15.01	35	13.74	28	15.74	35	16.42	33

Table 7

	dT/dt	Net Condensation	Large-scale Forcing	Net Q_{R}=SW-LW	Sensible Heat Fluxes
TOGA COARE 1	-0.29	5.06	-5.55	0.03	0.17
TOGA COARE 2	-0.28	4.33	-4.61	-0.11	0.11
GATE	-0.20	3.13	-2.67	-0.68	0.02
ARM 1	0.83	2.16	-1.01	-0.63	0.31
ARM 2	0.67	1.37	-0.41	-0.51	0.22
ARM 3	-0.16	1.28	-1.05	-0.66	0.27

Table 8

Run	d(Qv) /dt	Net Condensation	Large-scale Forcing	Latent Heat Fluxes
TOGA COARE 1	0.57	-20.15	15.03	5.69
TOGA COARE 2	-0.80	-17.31	13.47	3.04
GATE	-0.33	-12.30	9.90	2.07
ARM 1	1.24	-8.13	5.29	4.08
ARM 2	-0.02	-5.07	1.19	3.86
ARM 3	0.31	-4.83	0.80	4.34

Table 9

	D(CpT+ LvQv)	Net Condensation	Large-scale Forcing	Net Q_R	Sensible Heat Fluxes	Latent Heat Fluxes
TOGA COARE 1	-16.71	0.49	-204.96	3.34	19.76	164.66
TOGA COARE 2	-55.25	-0.98	-142.57	-12.75	13.24	87.91
GATE	-32.27	4.48	-21.14	-77.69	2.35	59.73
ARM 1	126.35	0.75	42.91	-68.93	33.62	118.00
ARM 2	72.24	2.14	-10.54	-54.96	23.85	111.75
ARM 3	-8.27	-0.78	-90.75	-72.19	29.74	125.71

Table 10

Run	Precipitation Efficiency (PE)	Rainfall (mm/day)	Condensation (mm/day)
SCSMEX 1 (May)	45.4	11.14	24.56
SCSMEX 2 (June)	45.3	16.46	36.31
TOGA COARE 1	41.6	20.15	48.39
TOGA COARE 2	37.5	17.81	47.52
GATE	44.5	12.31	27.67
ARM 1	40.1	7.51	18.72
ARM 2	39.9	4.68	11.74
ARM 3	32.1	4.29	13.37

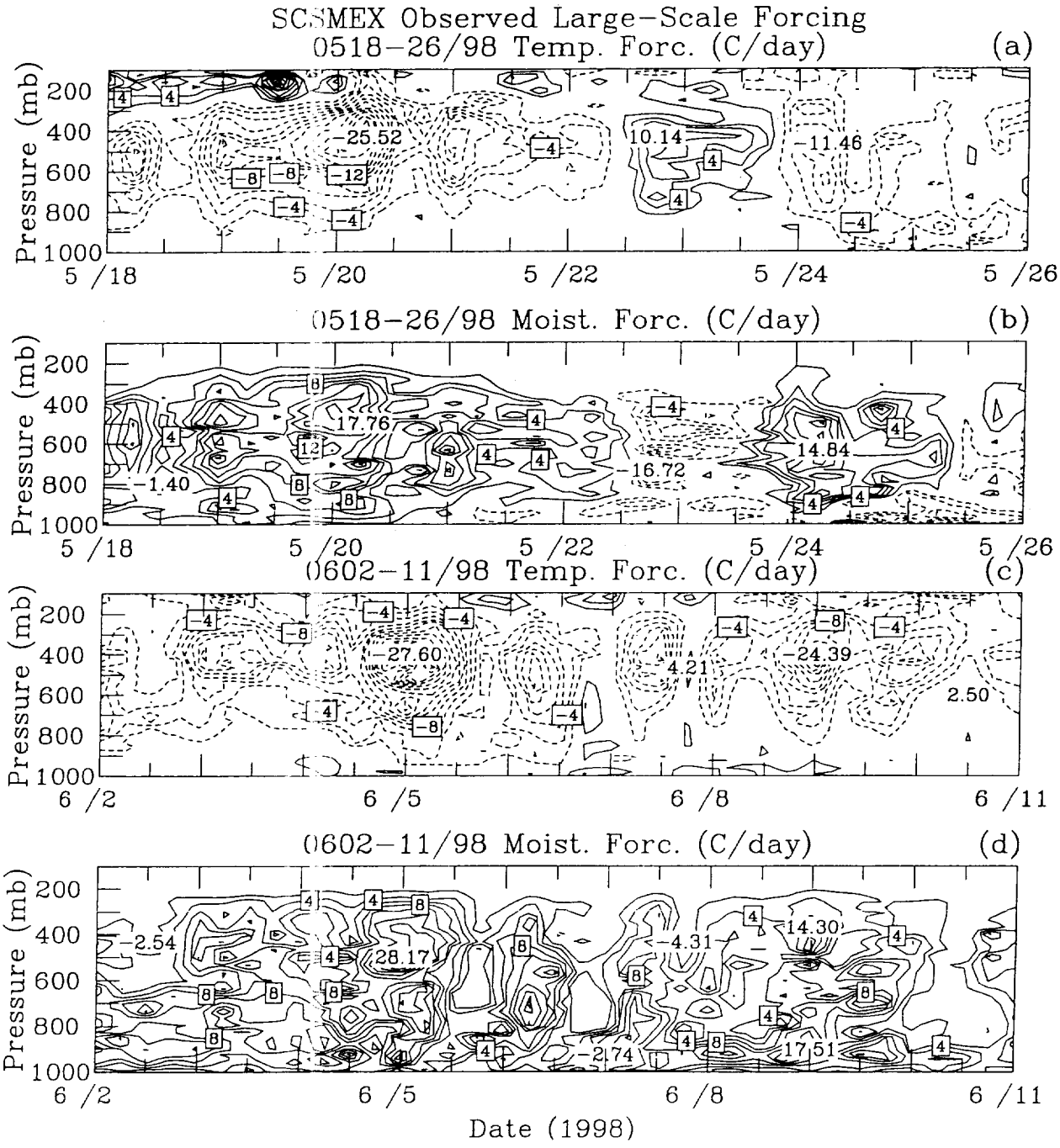
SCSMEX Observed Large-Scale Forcing
0518-26/98 Temp. Forc. (C/day)
(a)
Pressure (mb)
200
400
600
800
1000
-25.52
10.14
-11.46
5 /18
5 /20
5 /22
5 /24
5 /26
0518-26/98 Moist. Forc. (C/day)
(b)
17.76
-16.72
14.84
-1.40
0602-11/98 Temp. Forc. (C/day)
(c)
-27.60
4.21
-24.39
2.50
6 /2
6 /5
6 /8
6 /11
0602-11/98 Moist. Forc. (C/day)
(d)
-2.54
28.17
-4.31
14.30
-2.74
17.51
Date (1998)

Fig. 1

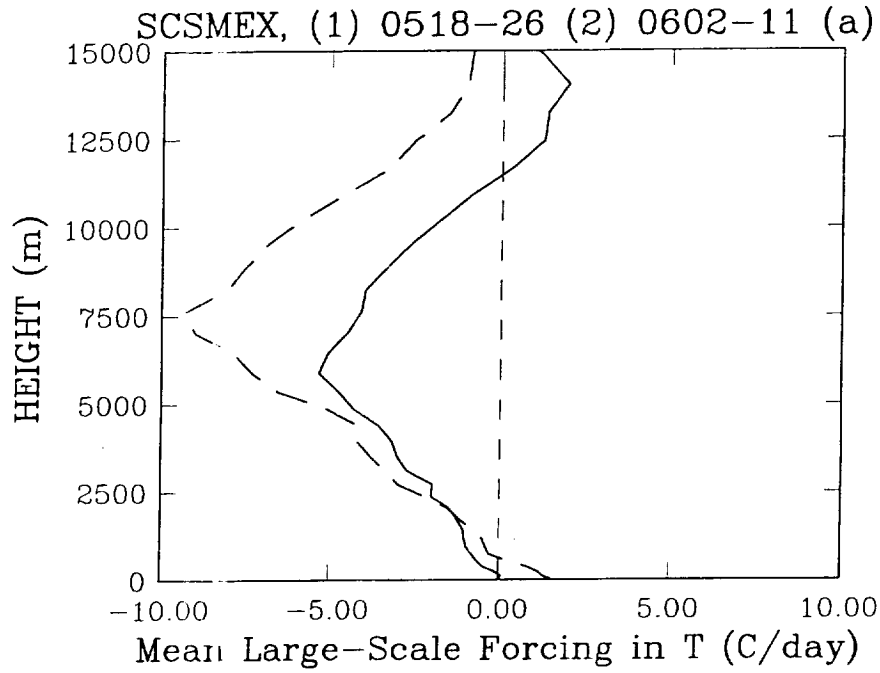
SCSMEX, (1) 0518–26 (2) 0602–11 (a)
HEIGHT (m)
15000
12500
10000
7500
5000
2500
0
−10.00
−5.00
0.00
5.00
10.00
Mean Large–Scale Forcing in T (C/day)

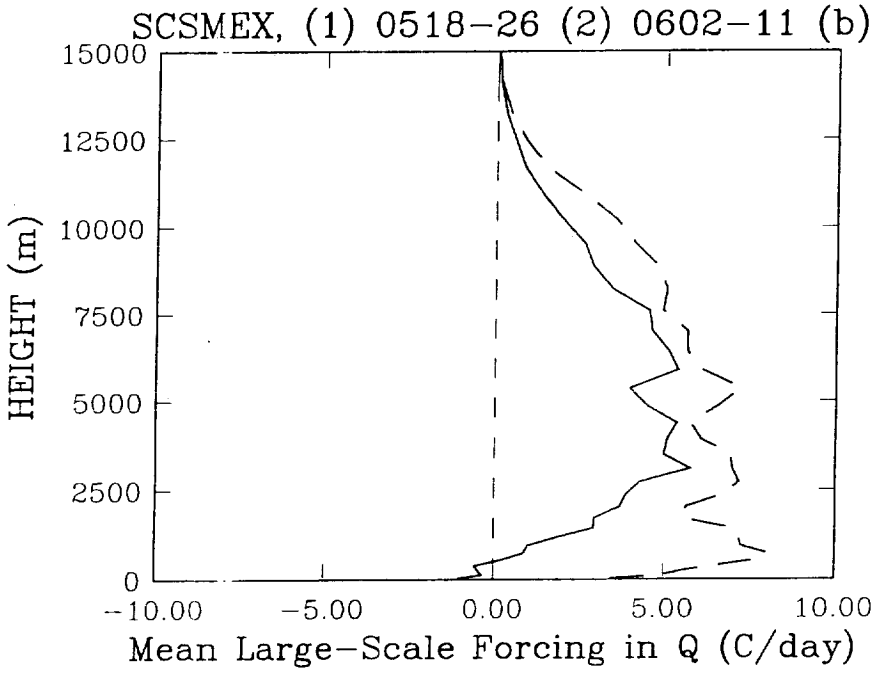
SCSMEX, (1) 0518–26 (2) 0602–11 (b)
HEIGHT (m)
15000
12500
10000
7500
5000
2500
0
−10.00
−5.00
0.00
5.00
10.00
Mean Large–Scale Forcing in Q (C/day)

Fig. 2

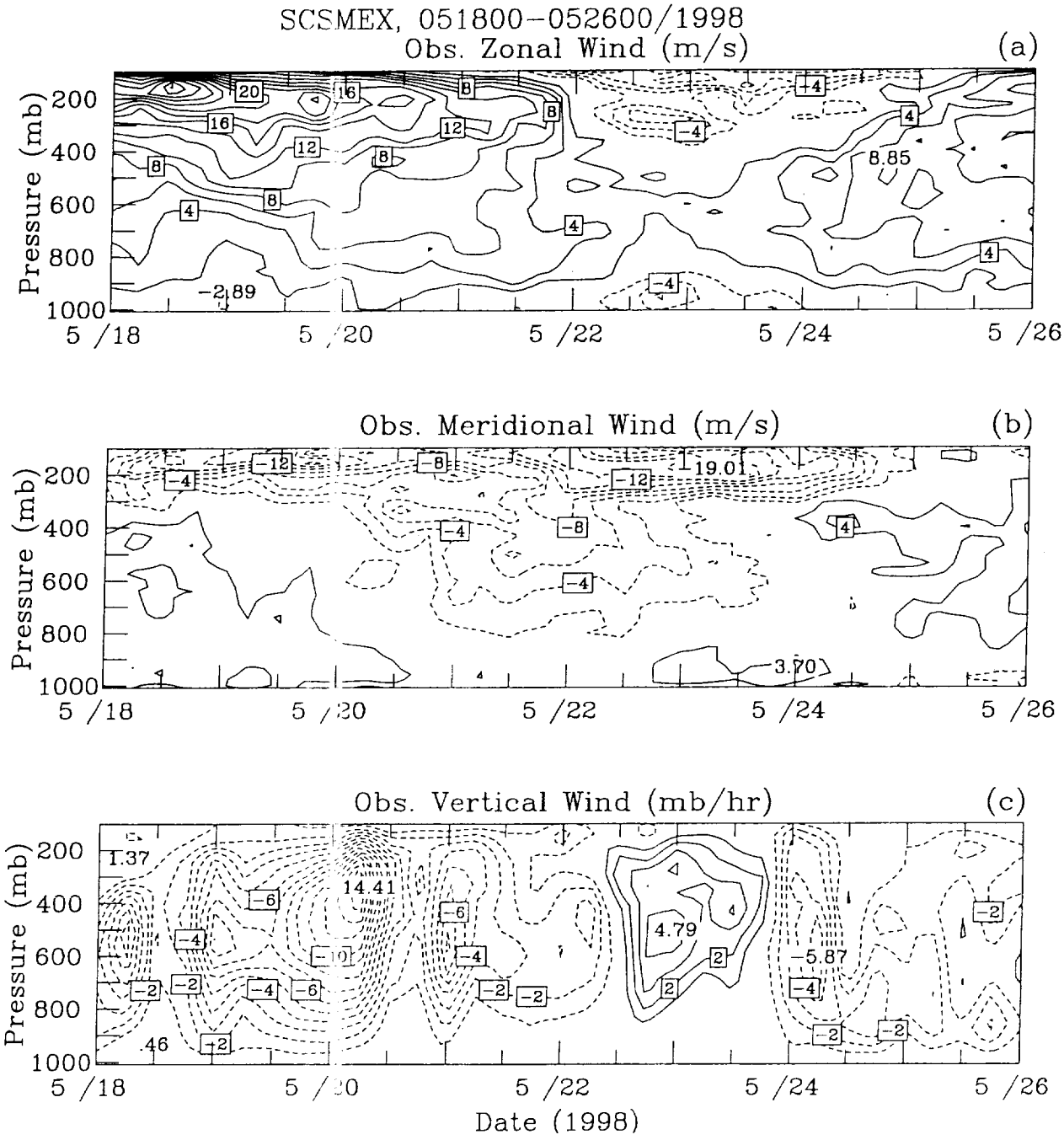
SCSMEX, 051800-052600/1998
Obs. Zonal Wind (m/s)
(a)
Pressure (mb)
200
400
600
800
1000
5 /18
5 /20
5 /22
5 /24
5 /26
8.85
-2.89
Obs. Meridional Wind (m/s)
(b)
19.01
3.70
Obs. Vertical Wind (mb/hr)
(c)
1.37
14.41
4.79
-5.87
.46
Date (1998)

Fig. 3

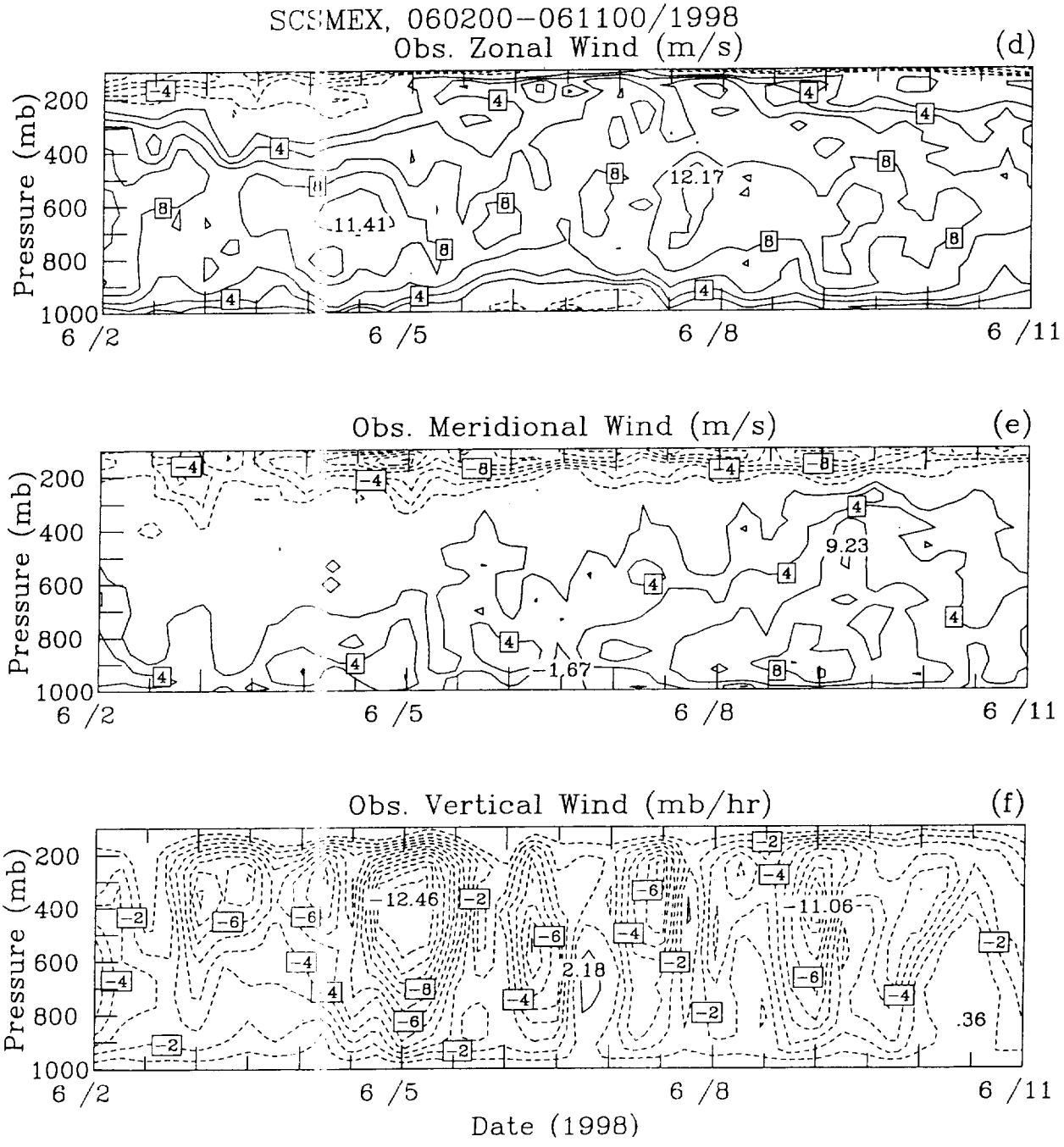
SCSMEX, 060200-061100/1998
Obs. Zonal Wind (m/s)
(d)
Pressure (mb)
200
400
600
800
1000
-11.41
12.17
6 /2
6 /5
6 /8
6 /11
Obs. Meridional Wind (m/s)
(e)
9.23
-1.67
Obs. Vertical Wind (mb/hr)
(f)
-12.46
2.18
-11.06
.36
Date (1998)

Fig. 3 (Cont.)

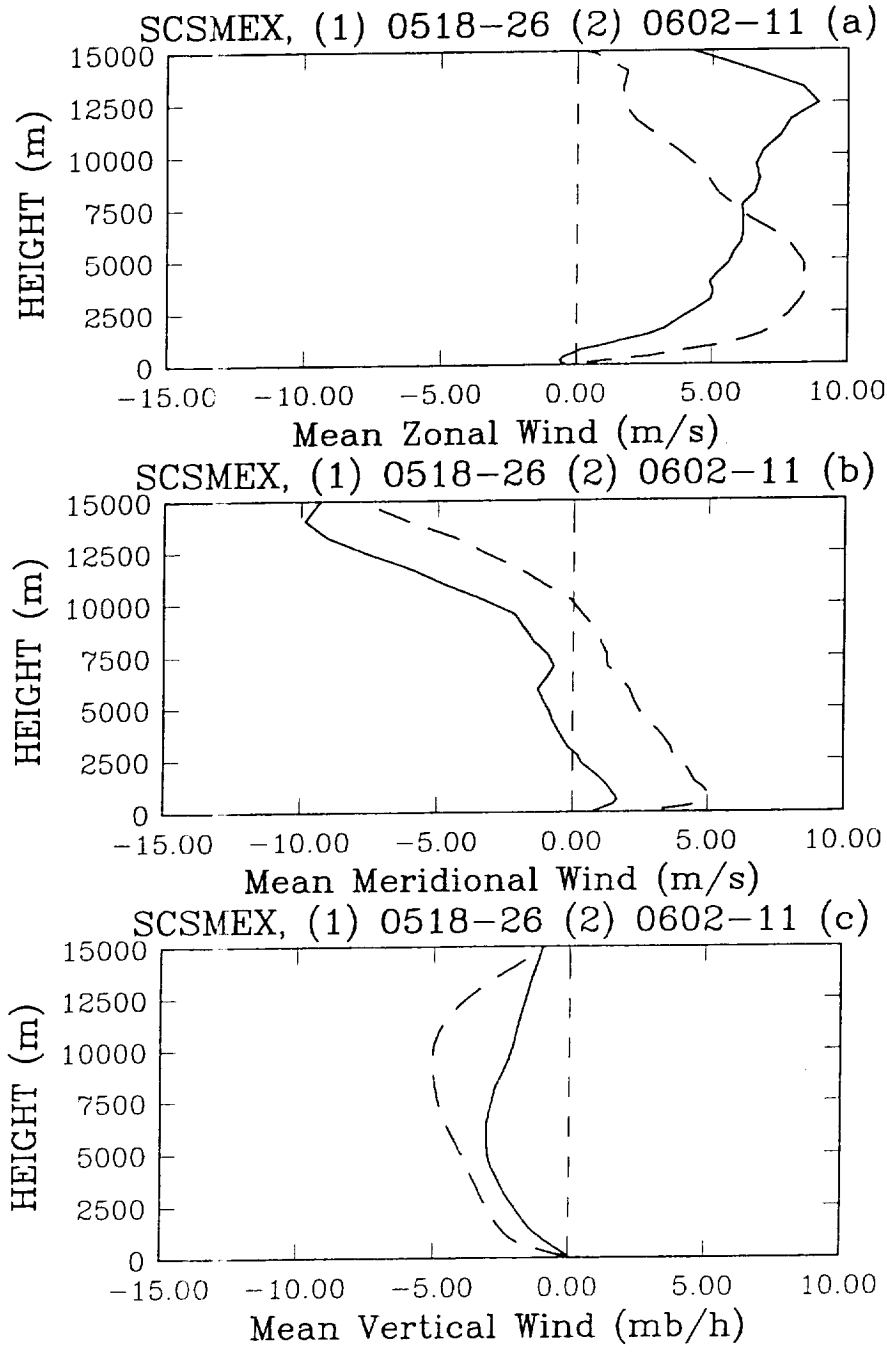
SCSMEX, (1) 0518–26 (2) 0602–11 (a)
HEIGHT (m)
15000
12500
10000
7500
5000
2500
0
−15.00
−10.00
−5.00
0.00
5.00
10.00
Mean Zonal Wind (m/s)
SCSMEX, (1) 0518–26 (2) 0602–11 (b)
HEIGHT (m)
Mean Meridional Wind (m/s)
SCSMEX, (1) 0518–26 (2) 0602–11 (c)
HEIGHT (m)
Mean Vertical Wind (mb/h)

Fig. 4

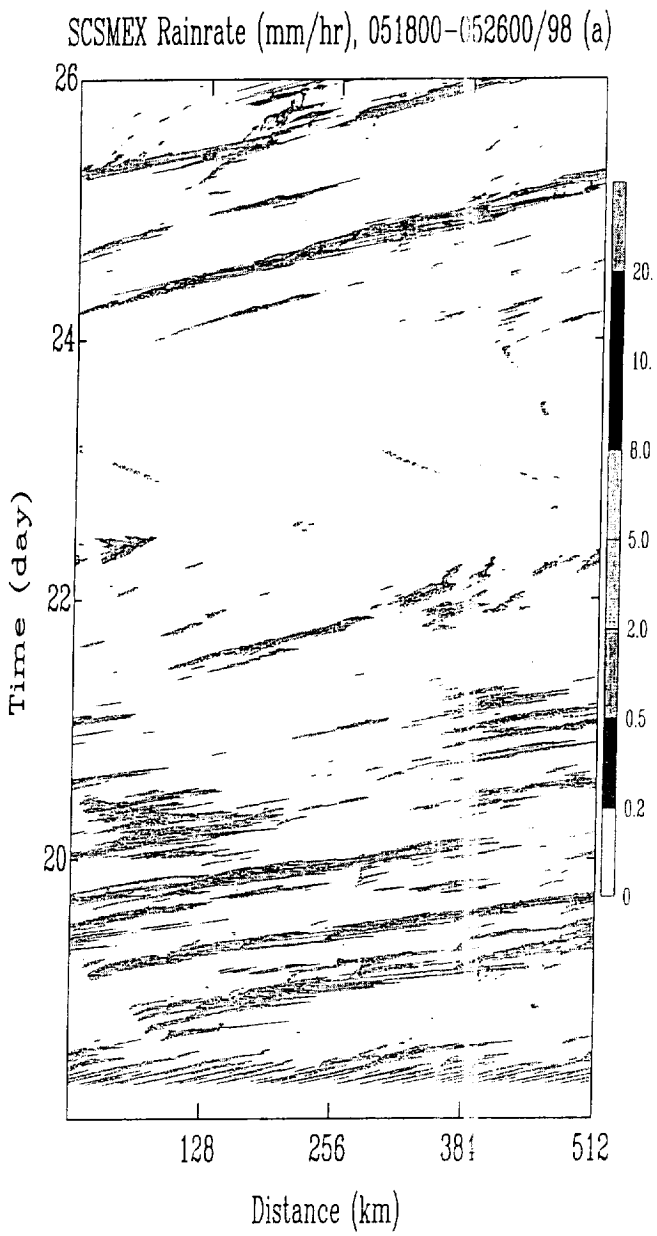
SCSMEX Rainrate (mm/hr), 051800-052600/98 (a)
26
24
22
20
Time (day)
20.
10.
8.0
5.0
2.0
0.5
0.2
0
128
256
384
512
Distance (km)

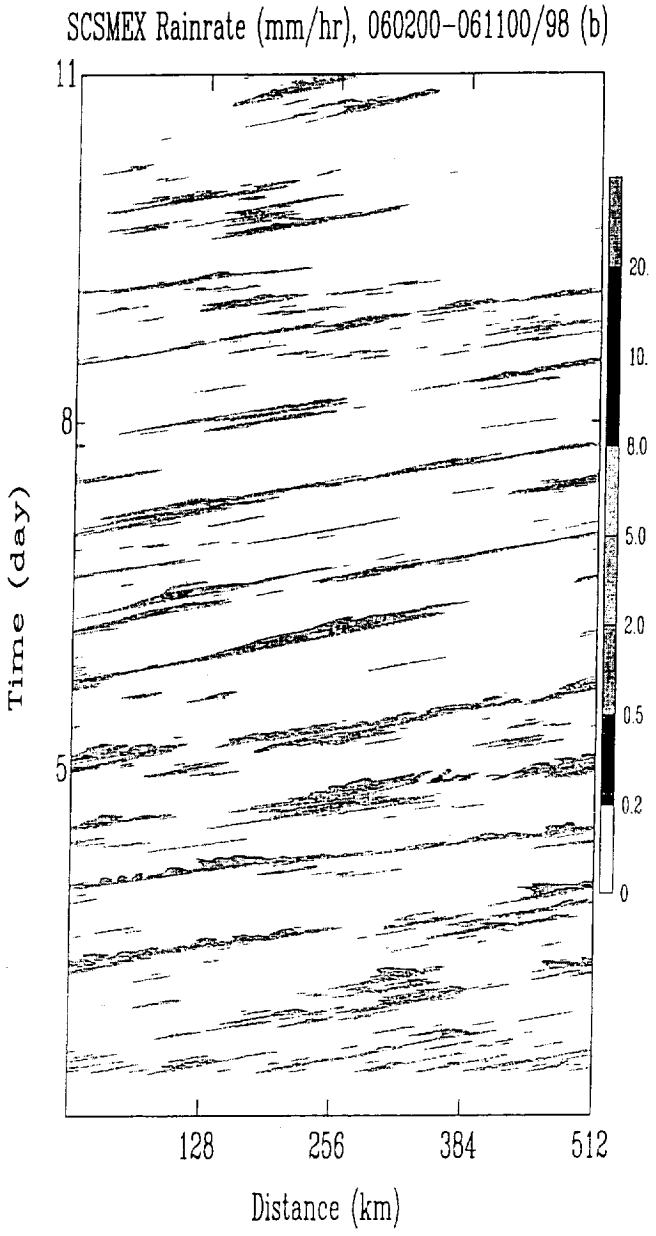
SCSMEX Rainrate (mm/hr), 060200-061100/98 (b)
11
8
5
Time (day)
20.
10.
8.0
5.0
2.0
0.5
0.2
0
128
256
384
512
Distance (km)

Fig. 5

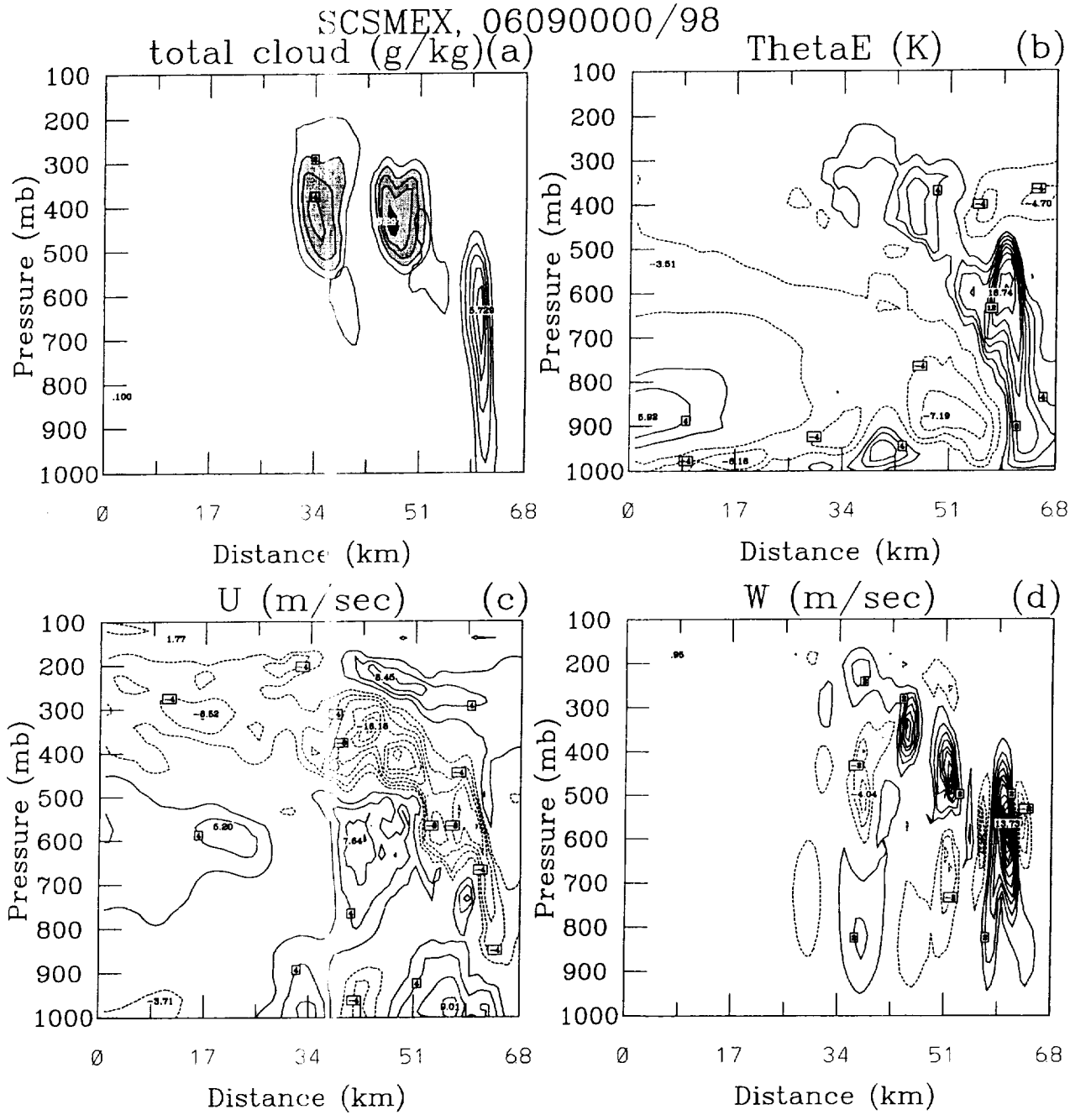
SCSMEX, 06090000/98
total cloud (g/kg)(a)
ThetaE (K) (b)
U (m/sec) (c)
W (m/sec) (d)
Pressure (mb)
100
200
300
400
500
600
700
800
900
1000
Ø
17
34
51
68
Distance (km)

Fig. 6

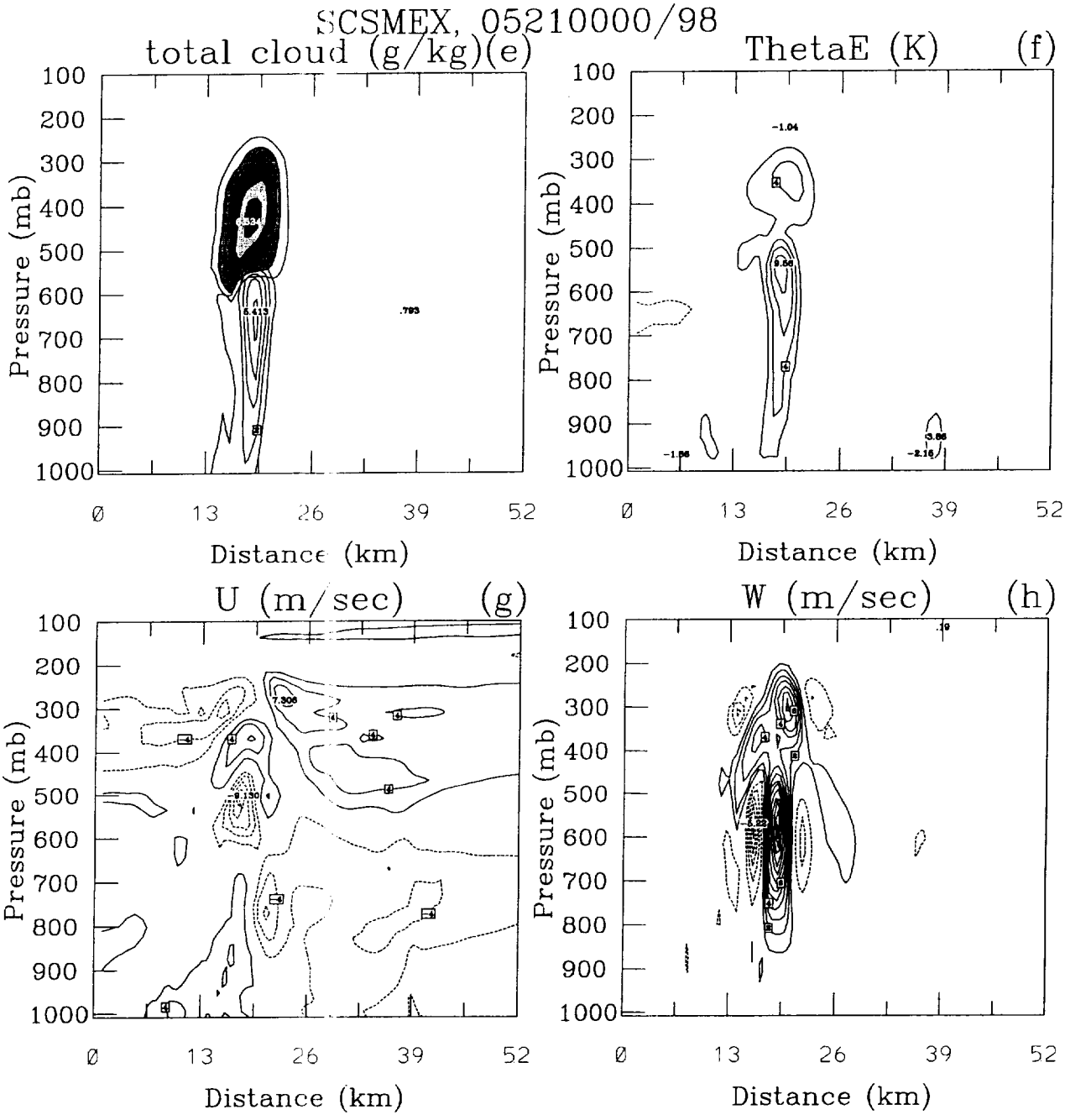
SCSMEX, 05210000/98
total cloud (g/kg)(e)
ThetaE (K) (f)
U (m/sec) (g)
W (m/sec) (h)
Pressure (mb)
100
200
300
400
500
600
700
800
900
1000
0
13
26
39
52
Distance (km)

Fig. 6 (Cont.)

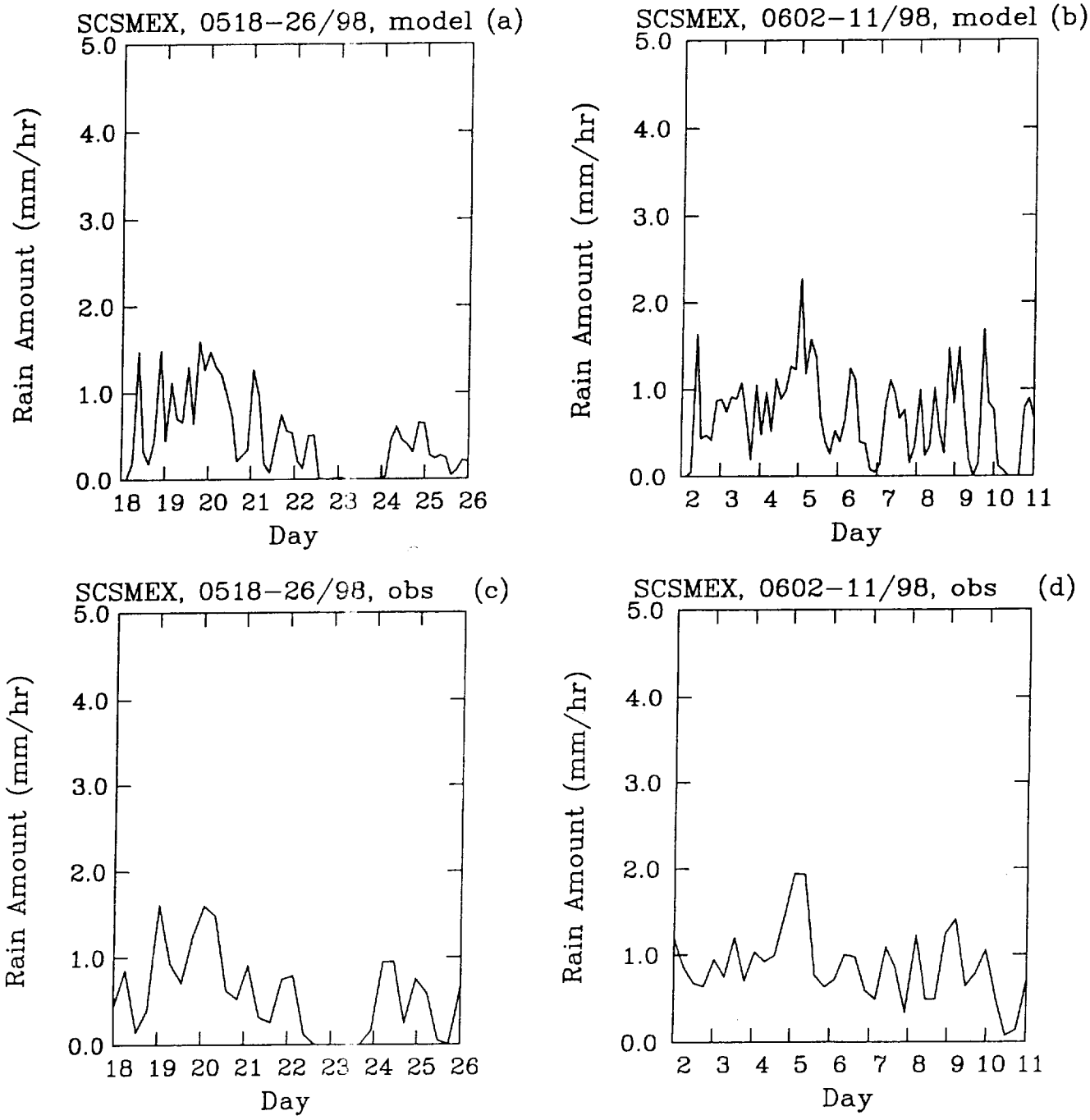
SCSMEX, 0518–26/98, model (a)
SCSMEX, 0602–11/98, model (b)
SCSMEX, 0518–26/98, obs (c)
SCSMEX, 0602–11/98, obs (d)
Rain Amount (mm/hr)
Day
5.0
4.0
3.0
2.0
1.0
0.0
18 19 20 21 22 23 24 25 26
2 3 4 5 6 7 8 9 10 11

Fig. 7

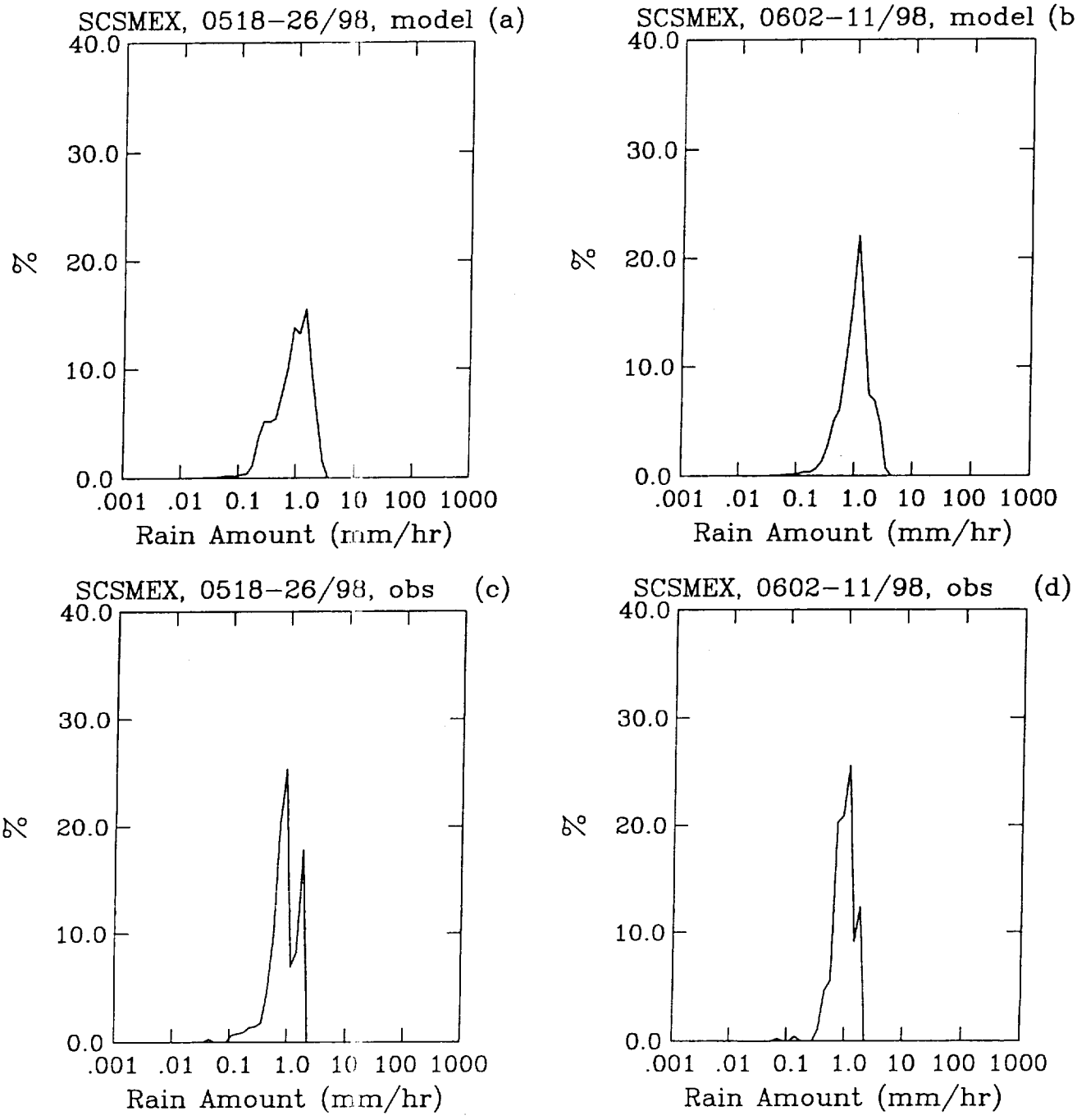
SCSMEX, 0518–26/98, model (a)
SCSMEX, 0602–11/98, model (b)
SCSMEX, 0518–26/98, obs (c)
SCSMEX, 0602–11/98, obs (d)
%
40.0
30.0
20.0
10.0
0.0
.001 .01 0.1 1.0 10 100 1000
Rain Amount (mm/hr)

Fig. 8

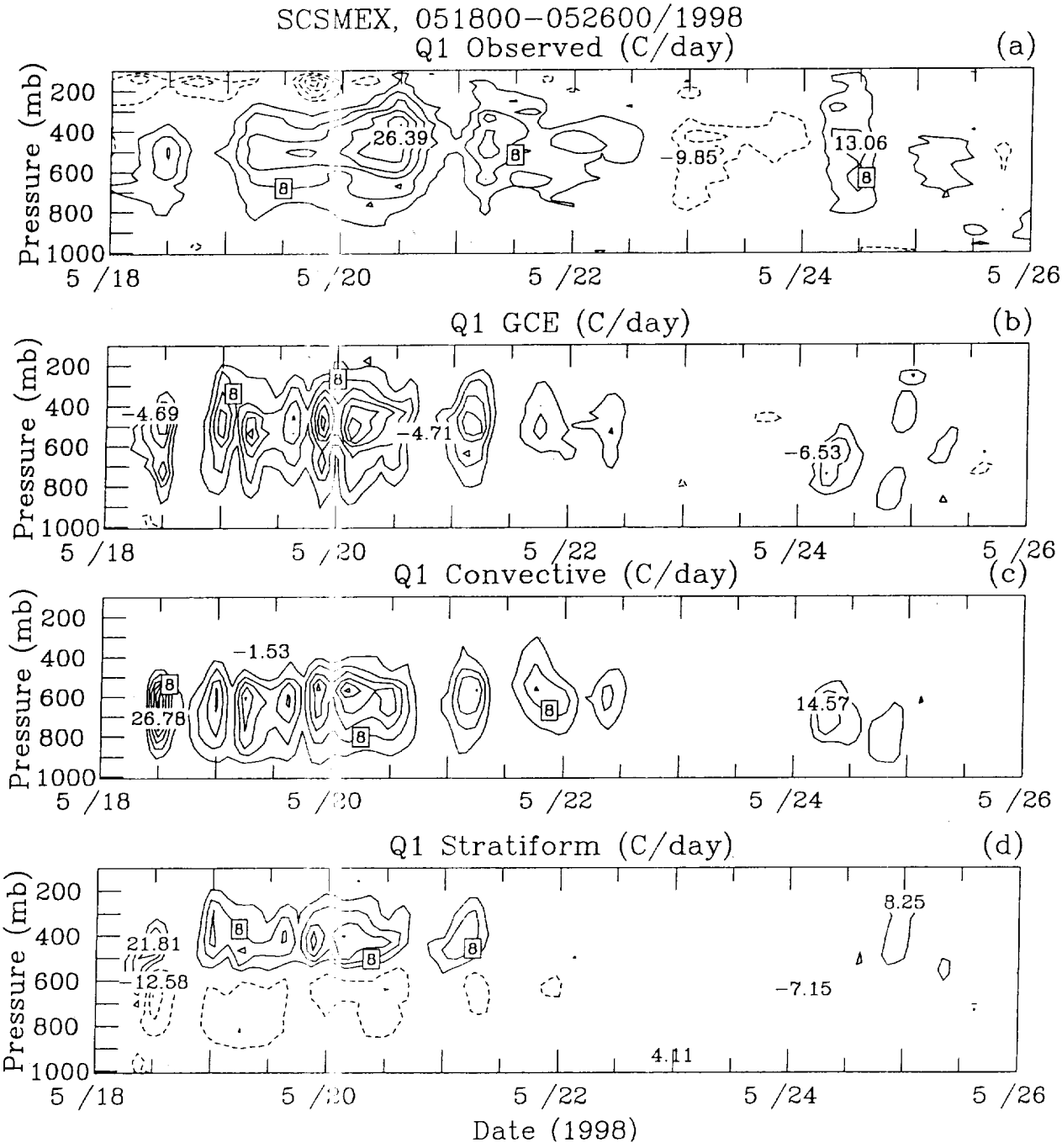
SCSMEX, 051800-052600/1998
Q1 Observed (C/day)
(a)
Pressure (mb)
200
400
600
800
1000
26.39
-9.85
13.06
5 /18
5 /20
5 /22
5 /24
5 /26
Q1 GCE (C/day)
(b)
-4.69
-4.71
-6.53
Q1 Convective (C/day)
(c)
-1.53
26.78
14.57
Q1 Stratiform (C/day)
(d)
21.81
-12.58
8.25
-7.15
4.11
Date (1998)

Fig. 9

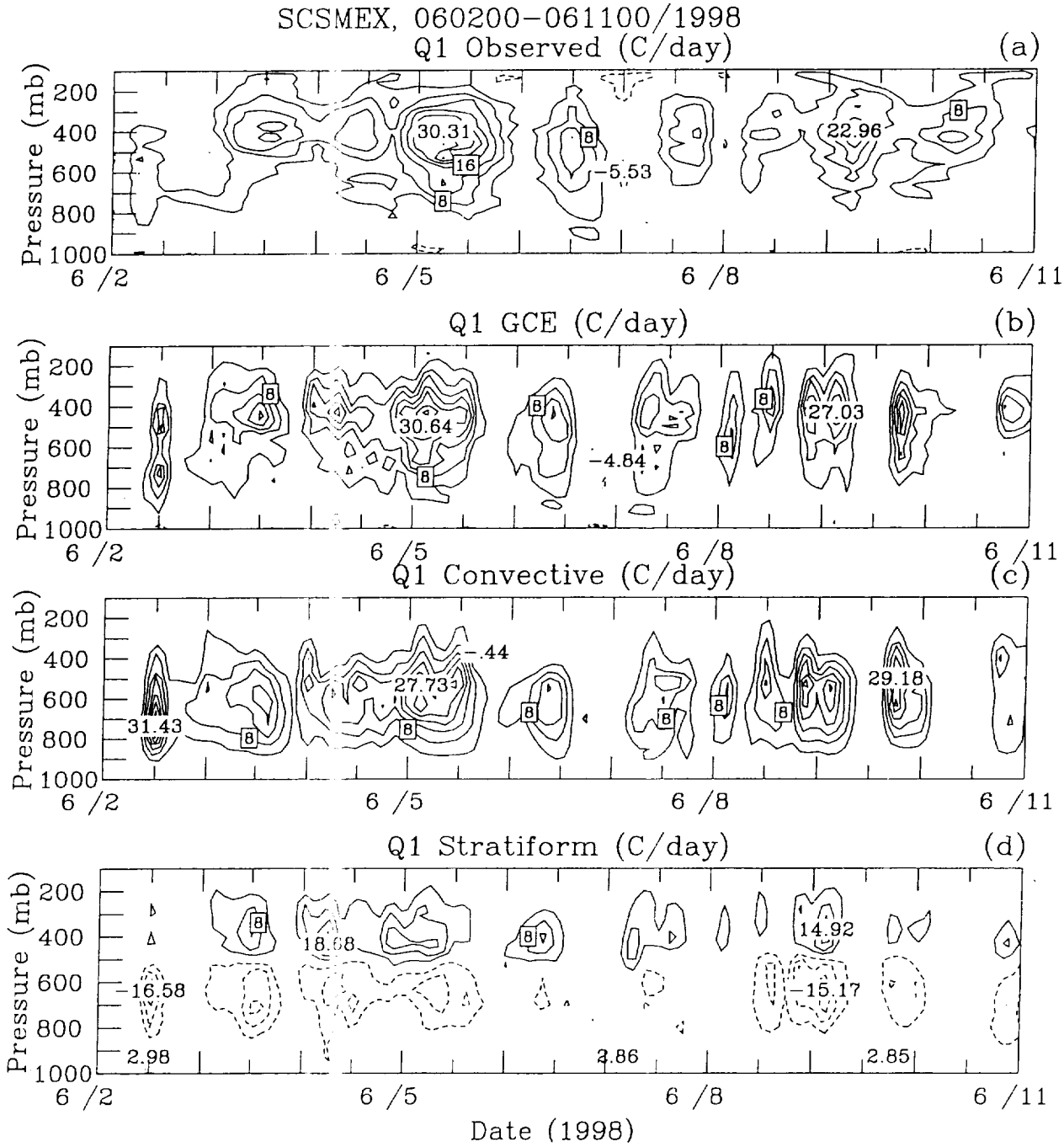
SCSMEX, 060200-061100/1998
Q1 Observed (C/day)
(a)
Pressure (mb)
200
400
600
800
1000
30.31
16
8
-5.53
22.96
6 /2
6 /5
6 /8
6 /11
Q1 GCE (C/day)
(b)
30.64
-4.84
27.03
Q1 Convective (C/day)
(c)
-.44
27.73
31.43
29.18
Q1 Stratiform (C/day)
(d)
18.68
14.92
-16.58
-15.17
2.98
3.86
2.85
Date (1998)

Fig. 10

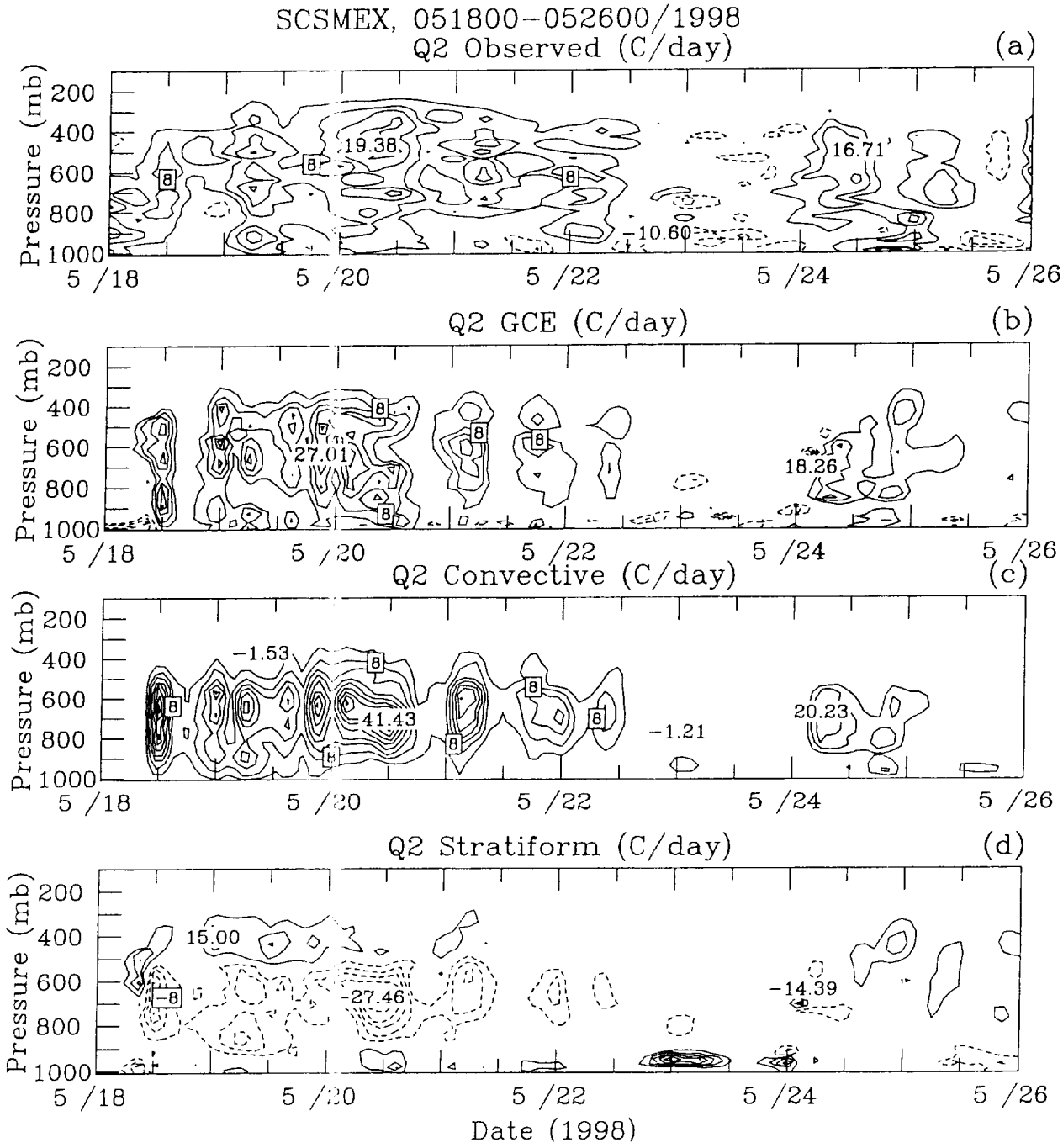
SCSMEX, 051800-052600/1998
Q2 Observed (C/day)
(a)
Pressure (mb)
200
400
600
800
1000
19.38
16.71
-10.60
5 /18
5 /20
5 /22
5 /24
5 /26
Q2 GCE (C/day)
(b)
27.01
18.26
Q2 Convective (C/day)
(c)
-1.53
41.43
-1.21
20.23
Q2 Stratiform (C/day)
(d)
15.00
-27.46
-14.39
Date (1998)

Fig. 11

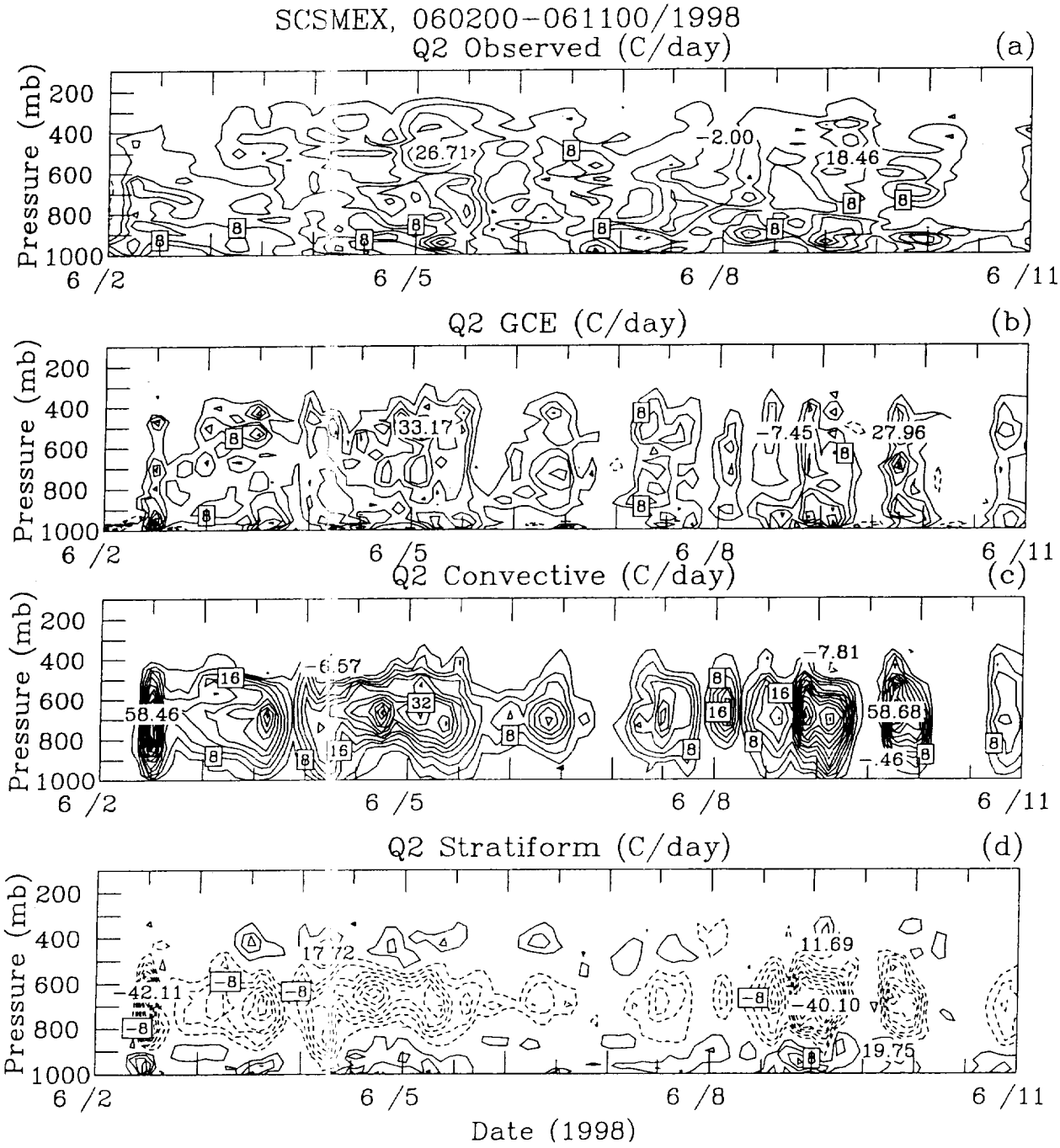
SCSMEX, 060200-061100/1998
Q2 Observed (C/day)
(a)
Pressure (mb)
200
400
600
800
1000
26.71
-2.00
18.46
6 /2
6 /5
6 /8
6 /11
Q2 GCE (C/day)
(b)
33.17
-7.45
27.96
Q2 Convective (C/day)
(c)
-6.57
-7.81
58.46
58.68
-.46
Q2 Stratiform (C/day)
(d)
17.72
11.69
-42.11
-40.10
19.75
Date (1998)

Fig. 12

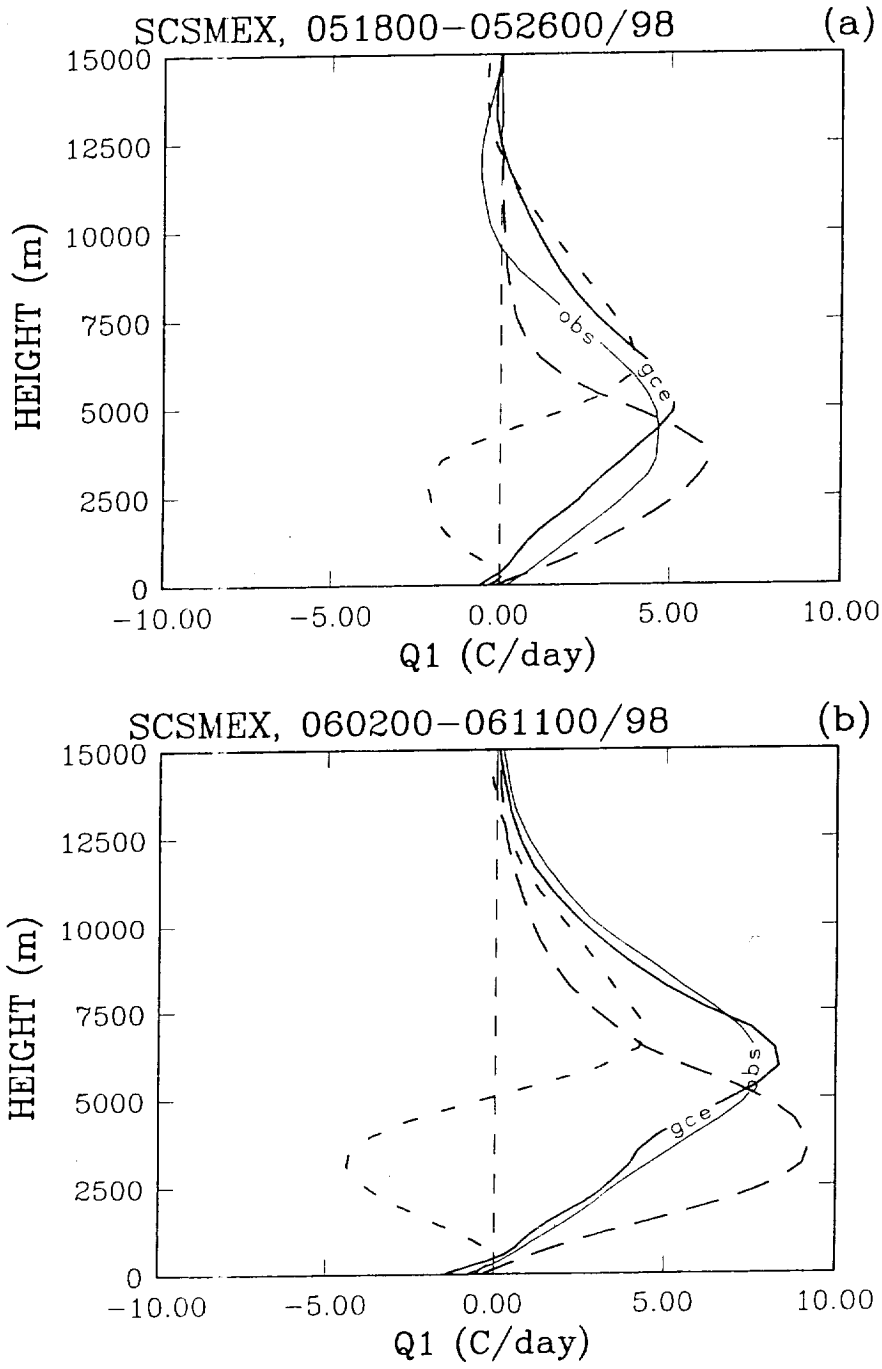
SCSMEX, 051800-052600/98
(a)
HEIGHT (m)
15000
12500
10000
7500
5000
2500
0
obs
gce
-10.00
-5.00
0.00
5.00
10.00
Q1 (C/day)
SCSMEX, 060200-061100/98
(b)
HEIGHT (m)
15000
12500
10000
7500
5000
2500
0
obs
gce
-10.00
-5.00
0.00
5.00
10.00
Q1 (C/day)

Fig. 13

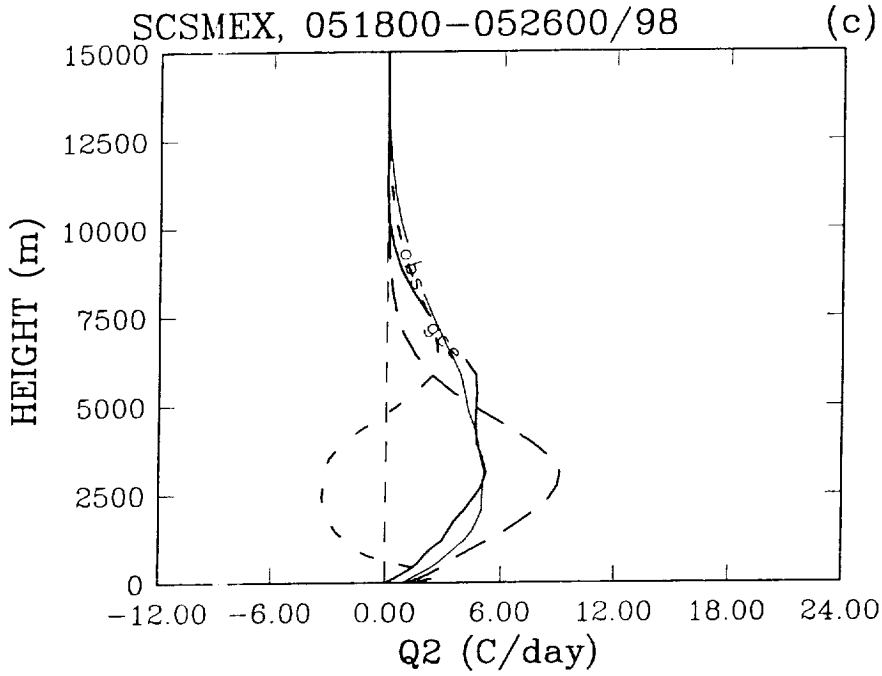
SCSMEX, 051800–052600/98
(c)
15000
12500
10000
7500
5000
2500
0
HEIGHT (m)
obs
gce
−12.00
-6.00
0.00
6.00
12.00
18.00
24.00
Q2 (C/day)

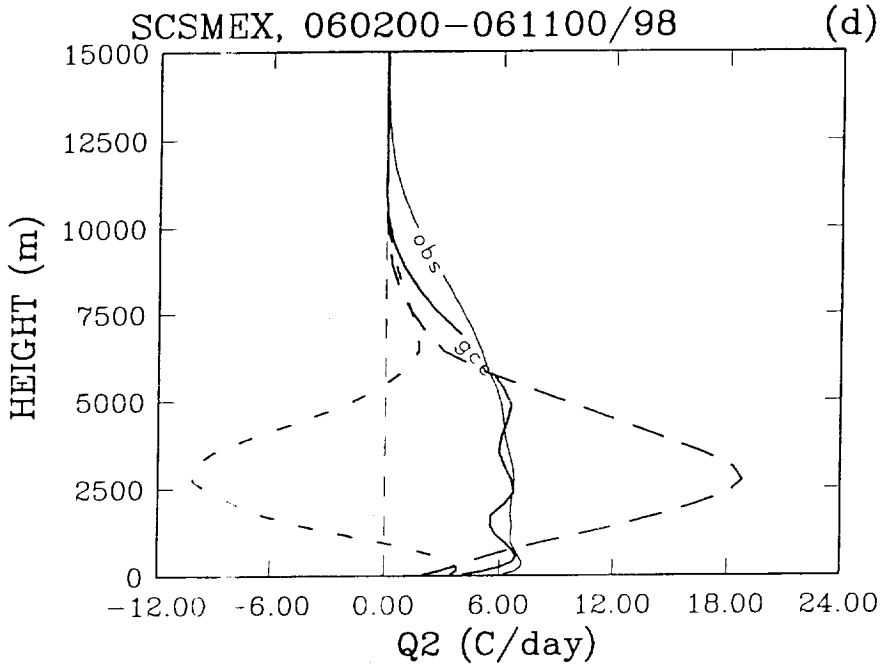
SCSMEX, 060200–061100/98
(d)
15000
12500
10000
7500
5000
2500
0
HEIGHT (m)
obs
gce
−12.00
-6.00
0.00
6.00
12.00
18.00
24.00
Q2 (C/day)

Fig. 13 (Cont.)

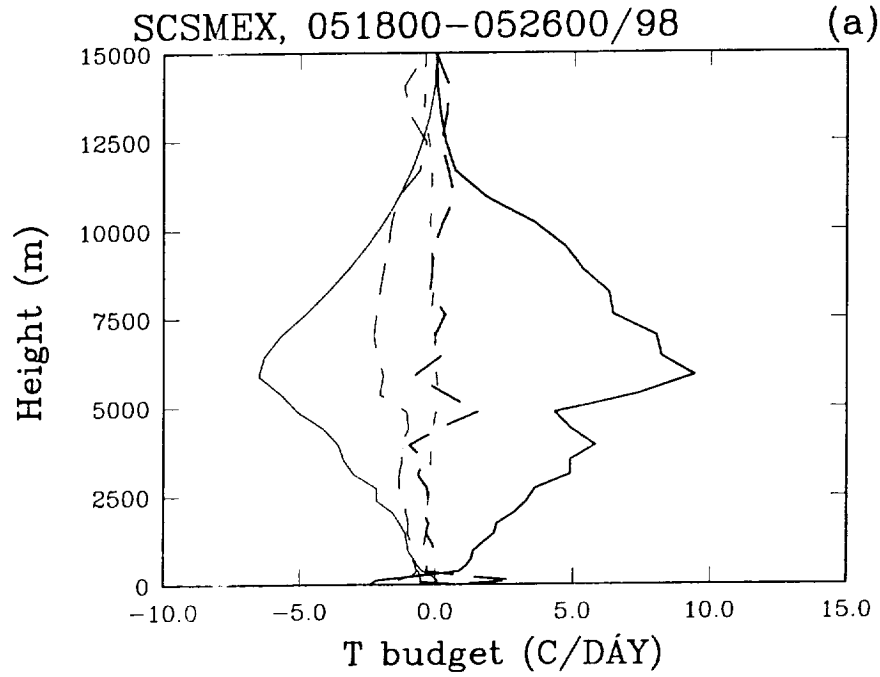
SCSMEX, 051800–052600/98
(a)
15000
12500
10000
7500
5000
2500
0
Height (m)
−10.0
−5.0
0.0
5.0
10.0
15.0
T budget (C/DAY)

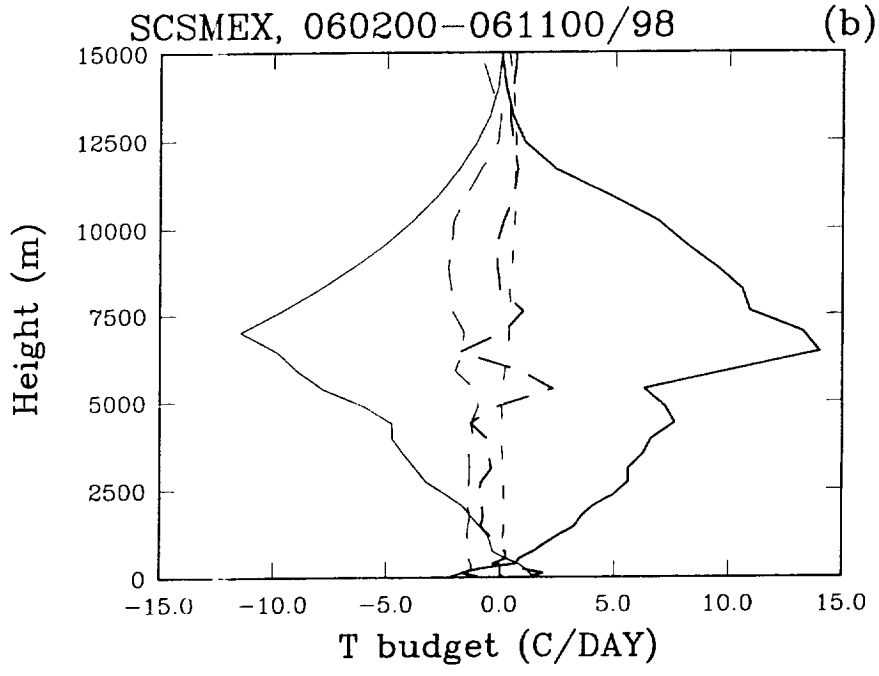
SCSMEX, 060200–061100/98
(b)
15000
12500
10000
7500
5000
2500
0
Height (m)
−15.0
−10.0
−5.0
0.0
5.0
10.0
15.0
T budget (C/DAY)

Fig. 14

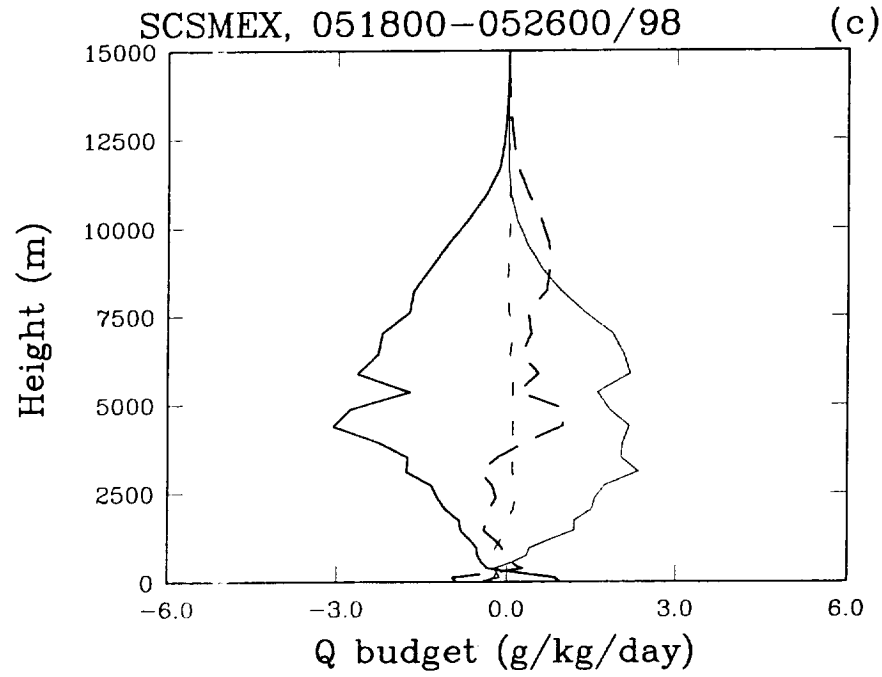
SCSMEX, 051800–052600/98
(c)
15000
12500
10000
7500
5000
2500
0
Height (m)
−6.0
−3.0
0.0
3.0
6.0
Q budget (g/kg/day)

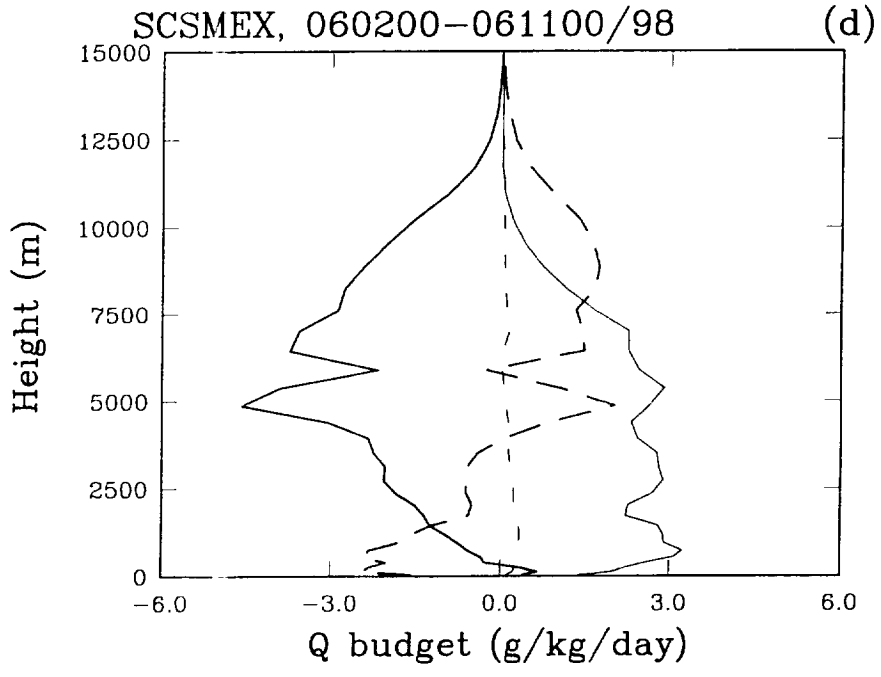
SCSMEX, 060200–061100/98
(d)
15000
12500
10000
7500
5000
2500
0
Height (m)
−6.0
−3.0
0.0
3.0
6.0
Q budget (g/kg/day)

Fig. 14 (Cont.)

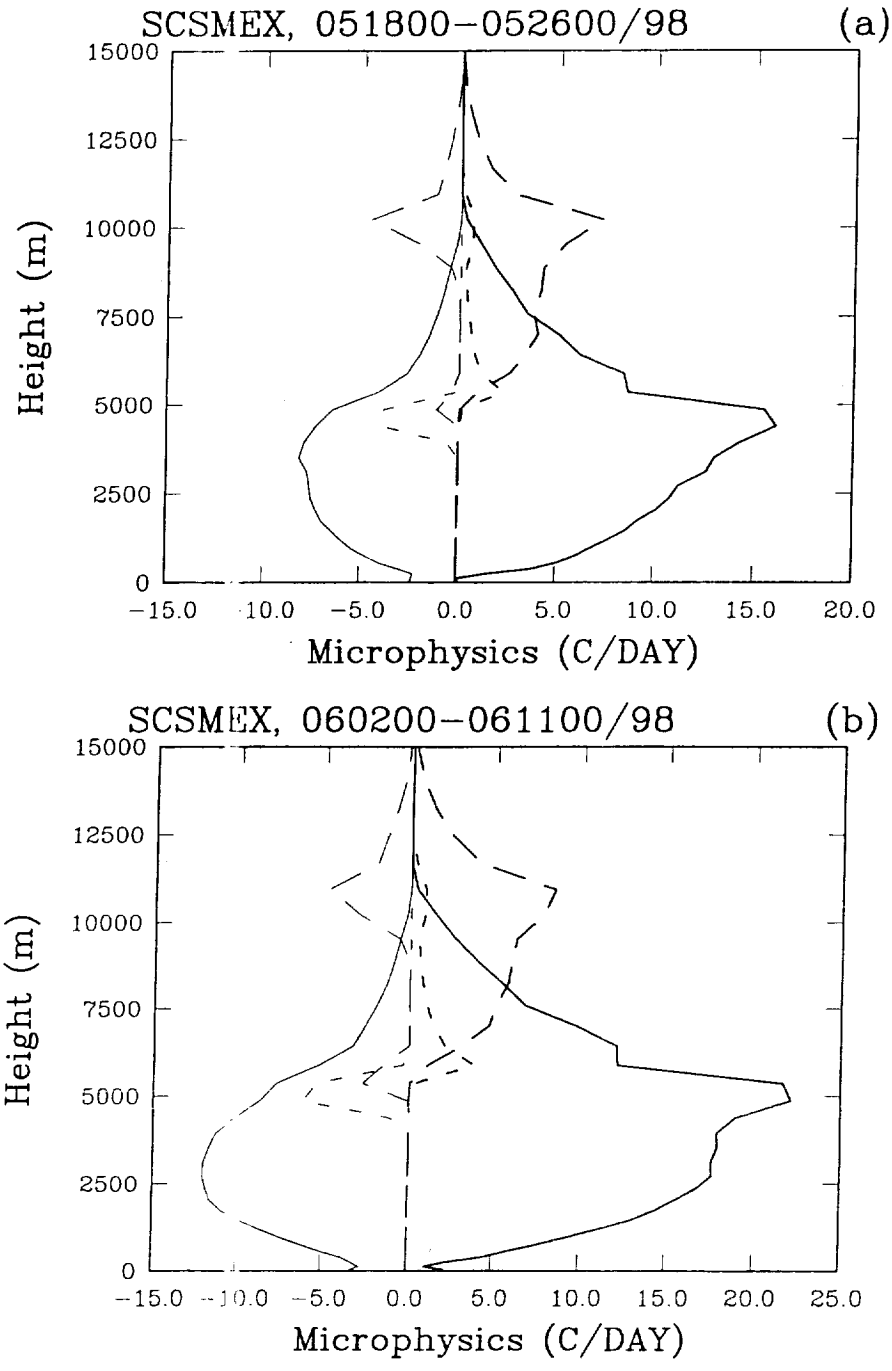
SCSMEX, 051800–052600/98
(a)
15000
12500
10000
7500
5000
2500
0
Height (m)
−15.0
−10.0
−5.0
0.0
5.0
10.0
15.0
20.0
Microphysics (C/DAY)
SCSMEX, 060200–061100/98
(b)
15000
12500
10000
7500
5000
2500
0
Height (m)
−15.0
−10.0
−5.0
0.0
5.0
10.0
15.0
20.0
25.0
Microphysics (C/DAY)

Fig. 15

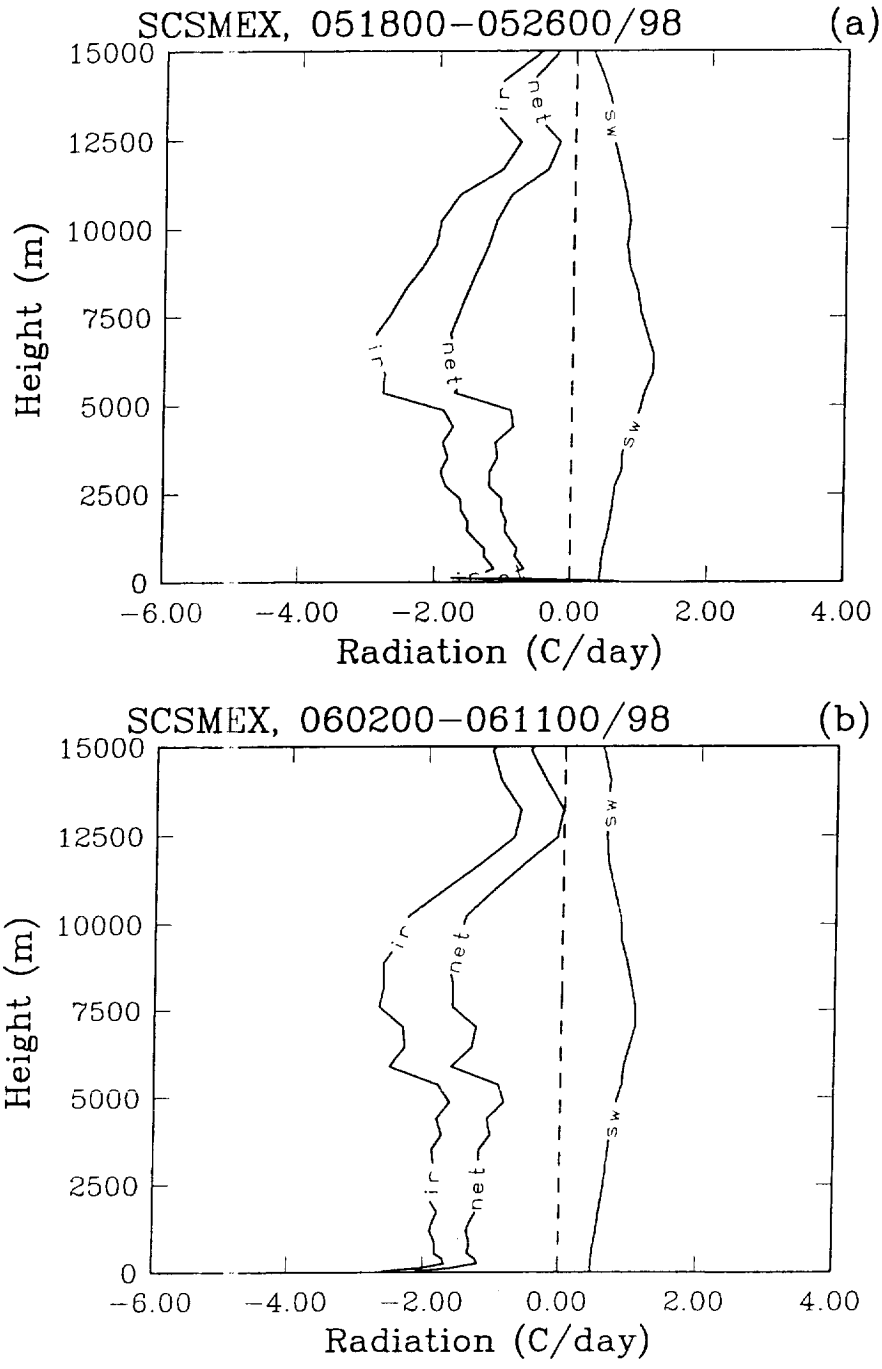
SCSMEX, 051800–052600/98
(a)
15000
12500
10000
7500
5000
2500
0
Height (m)
ir
net
sw
−6.00
−4.00
−2.00
0.00
2.00
4.00
Radiation (C/day)
SCSMEX, 060200–061100/98
(b)
15000
12500
10000
7500
5000
2500
0
Height (m)
ir
net
sw
−6.00
−4.00
−2.00
0.00
2.00
4.00
Radiation (C/day)

Fig. 16

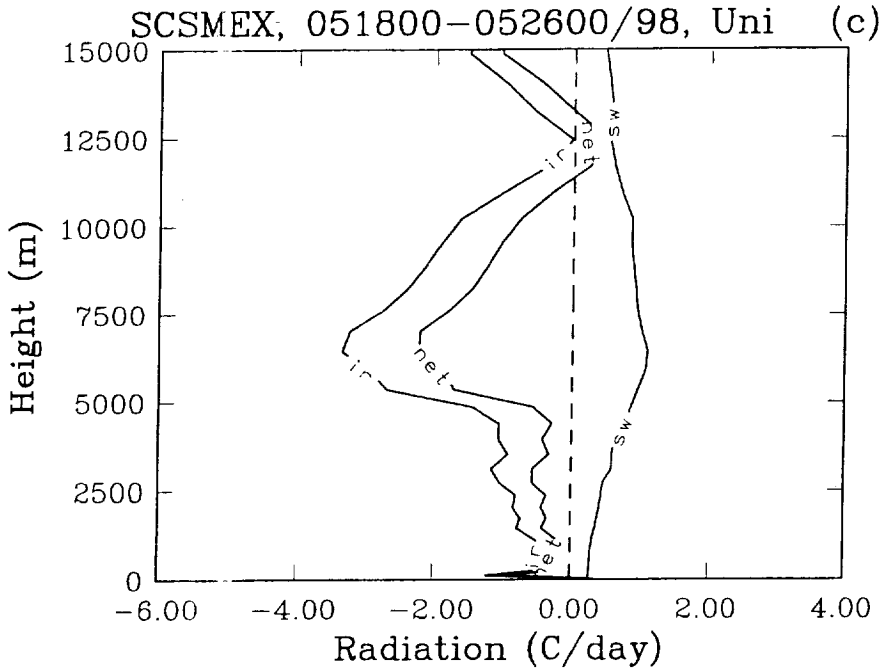
SCSMEX, 051800-052600/98, Uni (c)
15000
12500
10000
7500
5000
2500
0
Height (m)
-6.00
-4.00
-2.00
0.00
2.00
4.00
Radiation (C/day)
sw
net
ir

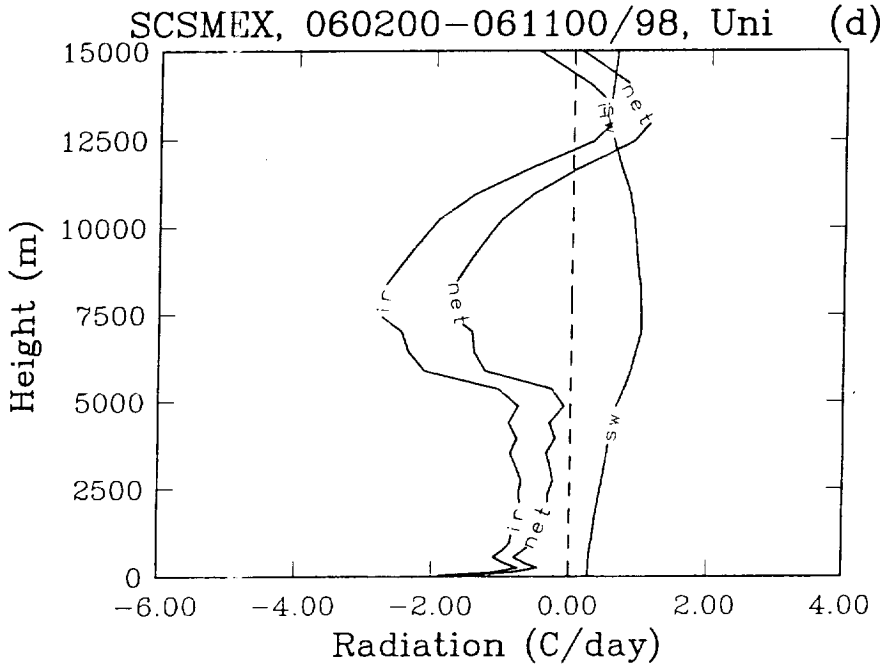
SCSMEX, 060200-061100/98, Uni (d)
15000
12500
10000
7500
5000
2500
0
Height (m)
-6.00
-4.00
-2.00
0.00
2.00
4.00
Radiation (C/day)
sw
net
ir

Fig. 16 (Cont.)

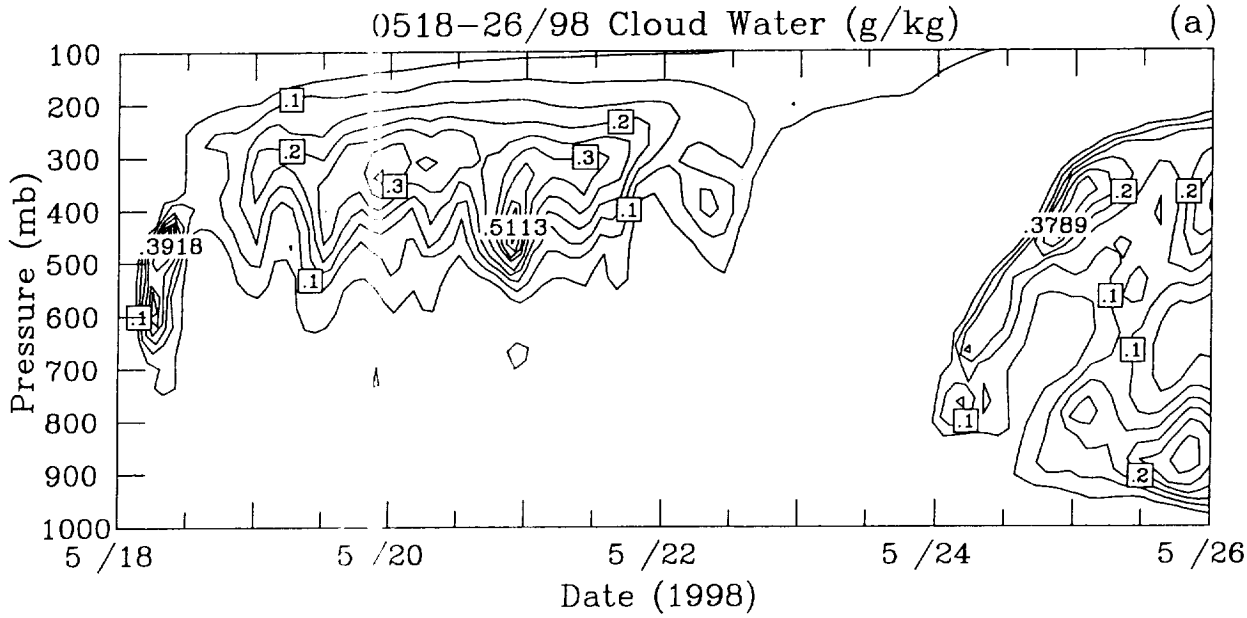
0518-26/98 Cloud Water (g/kg)
(a)
Pressure (mb)
100
200
300
400
500
600
700
800
900
1000
5 /18
5 /20
5 /22
5 /24
5 /26
Date (1998)
.3918
.5113
.3789

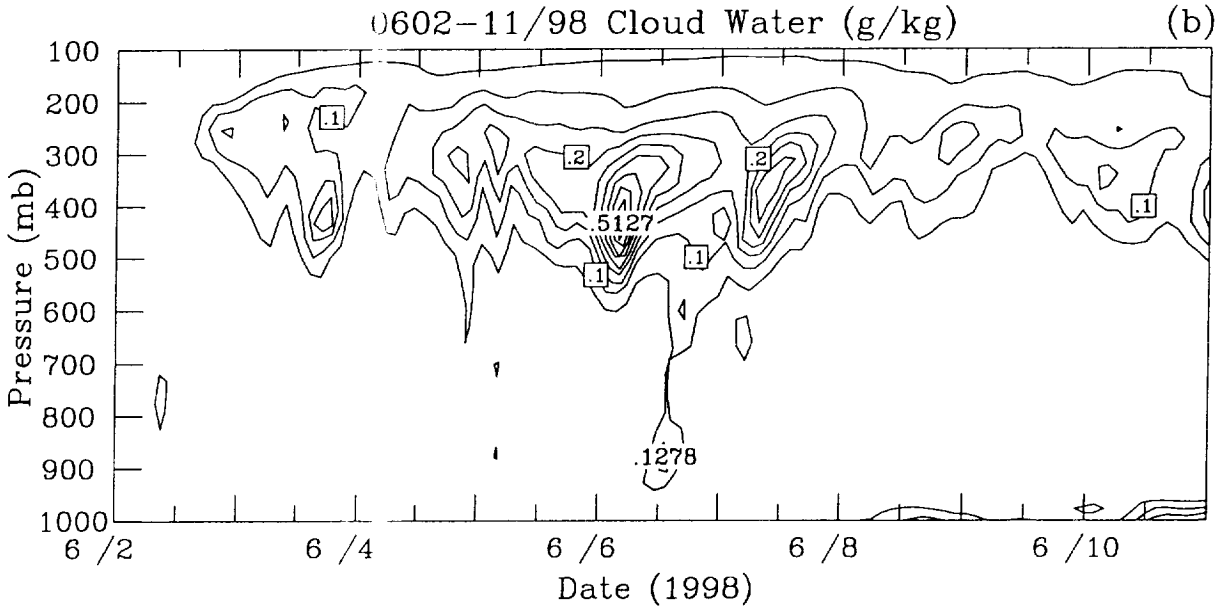
0602-11/98 Cloud Water (g/kg)
(b)
Pressure (mb)
100
200
300
400
500
600
700
800
900
1000
6 /2
6 /4
6 /6
6 /8
6 /10
Date (1998)
.5127
.1278

Fig. 17

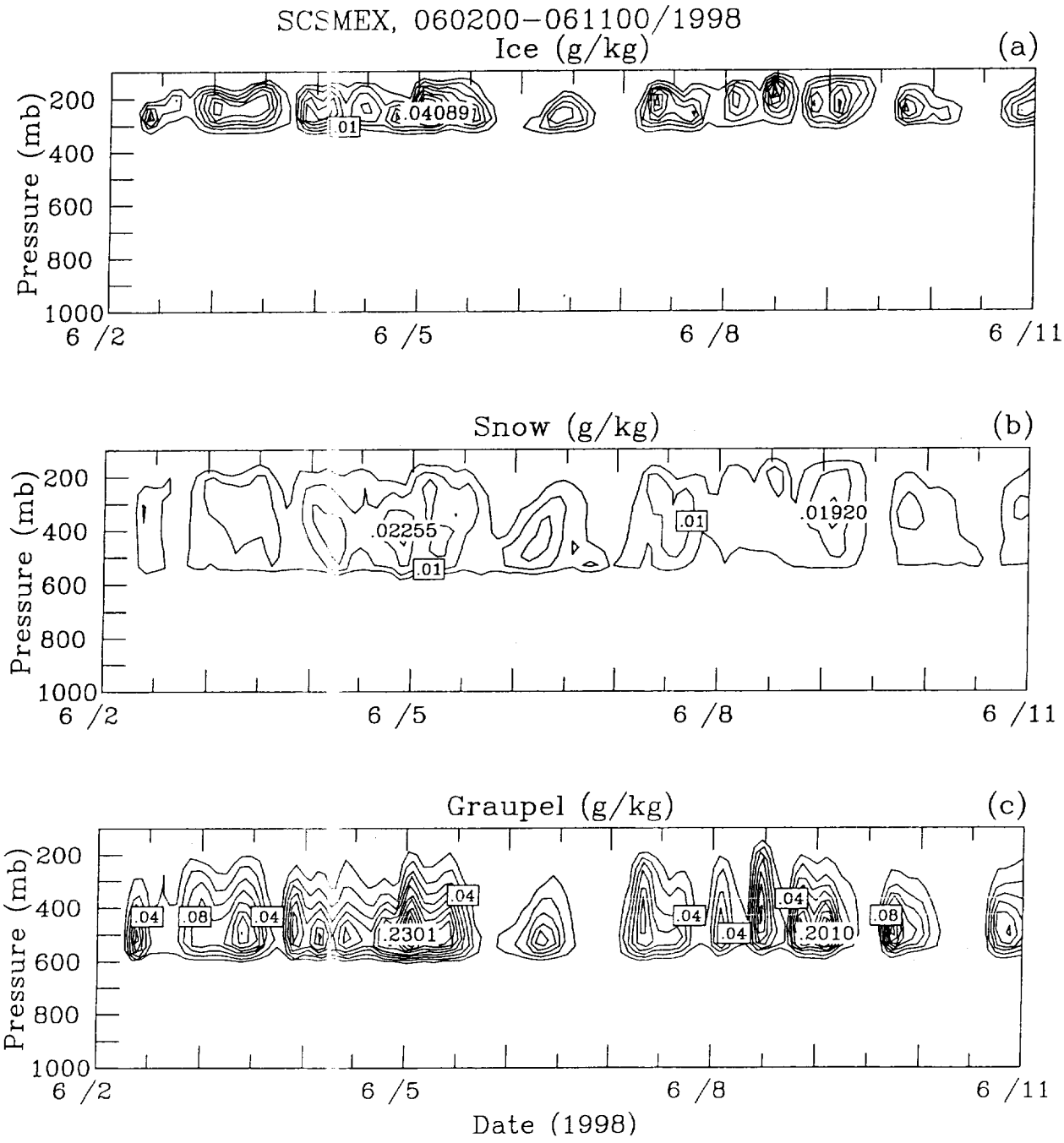
SCSMEX, 060200-061100/1998
Ice (g/kg)
(a)
Pressure (mb)
200
400
600
800
1000
.01
.04089
6 /2
6 /5
6 /8
6 /11
Snow (g/kg)
(b)
.02255
.01
.01
.01920
Graupel (g/kg)
(c)
.04
.08
.04
.04
.2301
.04
.04
.04
.2010
.08
Date (1998)

Fig. 18

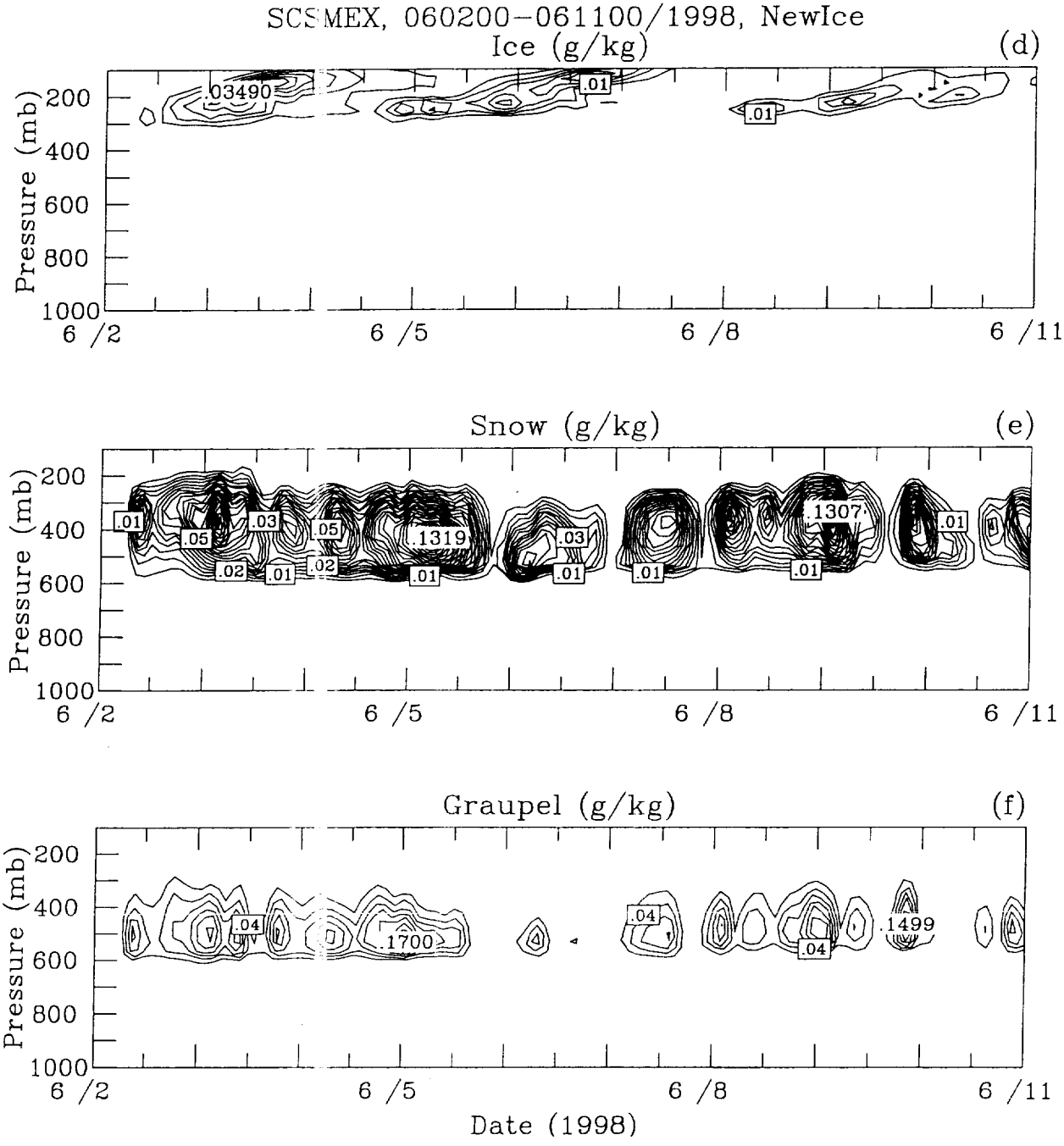
SCSMEX, 060200-061100/1998, NewIce
Ice (g/kg)
(d)
Pressure (mb)
200
400
600
800
1000
6 /2
6 /5
6 /8
6 /11
.03490
.01
.01
Snow (g/kg)
(e)
.01
.05
.03
.05
.1319
.02
.01
.02
.01
.03
.01
.01
.1307
.01
.01
Graupel (g/kg)
(f)
.04
.1700
.04
.04
.1499
Date (1998)

Fig. 18 (Cont.)

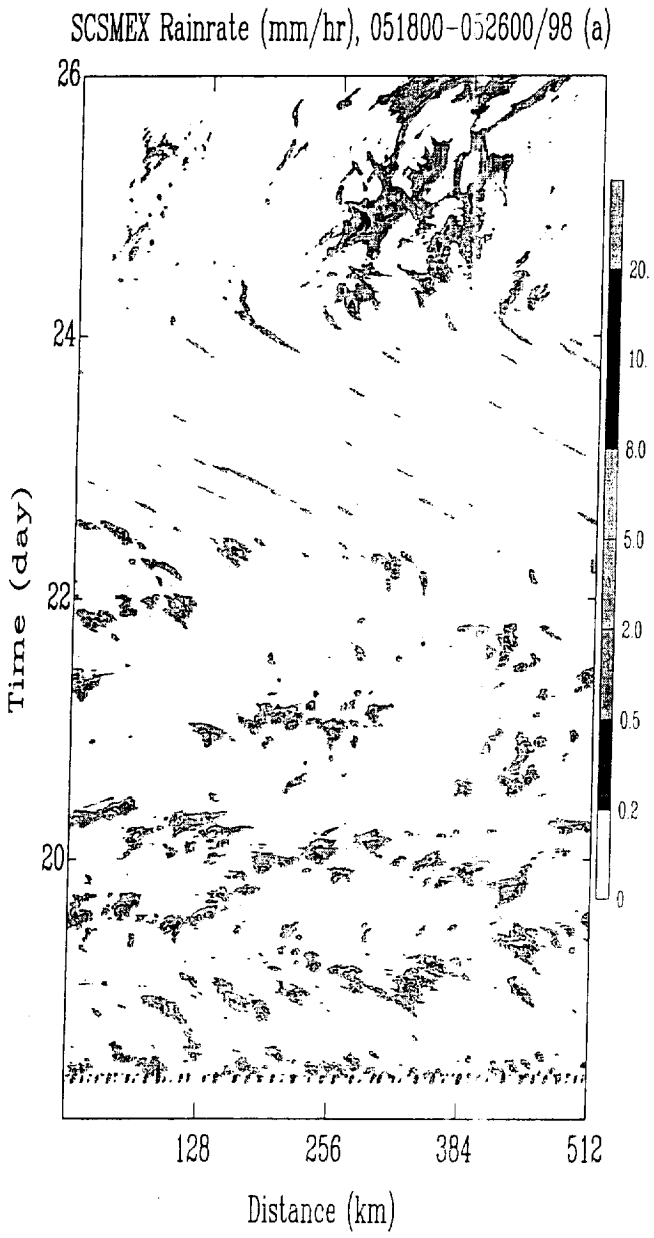
SCSMEX Rainrate (mm/hr), 051800-052600/98 (a)
26
24
22
20
Time (day)
20.
10.
8.0
5.0
2.0
0.5
0.2
0
128
256
384
512
Distance (km)

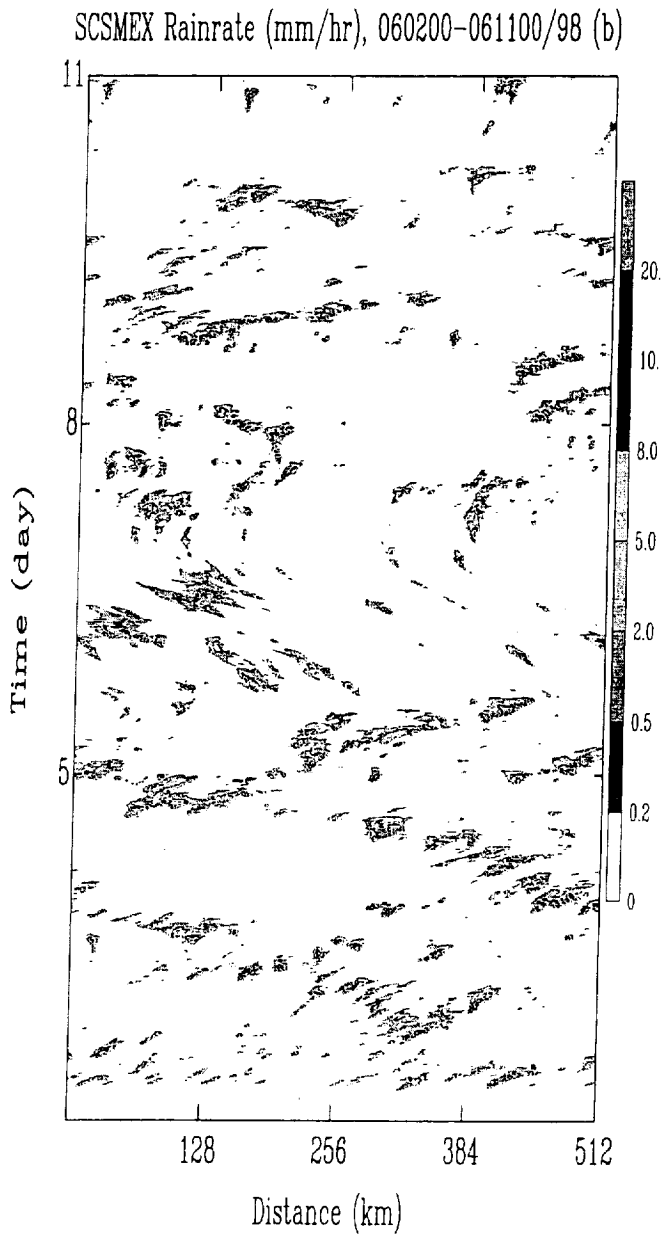
SCSMEX Rainrate (mm/hr), 060200-061100/98 (b)
11
8
5
Time (day)
20.
10.
8.0
5.0
2.0
0.5
0.2
0
128
256
384
512
Distance (km)

Fig. 19

Convective Systems over the South China Sea: Cloud-Resolving Model Simulations

W.-K. Tao, C.-L. Shie, D. Johnson, , J. Simpson, S. Braun, R. Johnson, and P. E. Ciesielski

Submitted to *Journal of Atmospheric Sciences*

Popular Summary

The South China Sea Monsoon Experiment (SCSMEX) was conducted in May-June 1998. One of its major objectives is to better understand the key physical processes for the onset and evolution of the summer monsoon over Southeast Asia and southern China. Multiple observation platforms (e.g., upper-air soundings, Doppler radar, ships, wind profilers, radiometers, etc.) during SCSMEX provided a first attempt at investigating the detailed characteristics of convective storms and air pattern changes associated with monsoons over the South China Sea region. SCSMEX also provided rainfall estimates which allows for comparisons with those obtained from the Tropical Rainfall Measuring Mission (TRMM), a low earth orbit satellite designed to measure rainfall from space.

The Goddard Cumulus Ensemble (GCE) model (with 1-km grid size) is used to understand and quantify the precipitation processes associated with the summer monsoon over the South China Sea. This is the first cloud-resolving model used to simulate precipitation processes in this particular region. The GCE-model results captured many of the observed precipitation characteristics because it used a fine grid size. For example, the temporal variation of the simulated rainfall compares quite well to the sounding-estimated rainfall variation. The time- and domain-averaged temperature (heating/cooling) and water vapor (drying/moistening) budgets are in good agreement with observations. The GCE-model-simulated rainfall amount also agrees well with TRMM rainfall data.

The results show there is more evaporation from the ocean surface prior to the onset of the monsoon than after the onset of monsoon when rainfall increases. Forcing due to net radiation (solar heating minus longwave cooling) is responsible for about 25% of the precipitation in SCSMEX. The transfer of heat from the ocean into the atmosphere does not contribute significantly to the rainfall in SCSMEX. Model sensitivity tests indicated that total rain production is reduced 17-18% in runs neglecting the ice phase.

The SCSMEX results are compared to other GCE-model-simulated weather systems that developed during other field campaigns (i.e., west Pacific warm pool region, eastern Atlantic region and central USA). Large-scale forcing vie temperature and water vapor tendency, is the major energy source for net condensation in the tropical cases. The effects of large-scale cooling exceed that of large-scale moistening in the west pacific warm pool region and eastern Atlantic region. For SCSMEX, however, the effects of large-scale moistening predominate. Net radiation and sensible and latent heat fluxes play a much more important role in the central USA.